Aerosol-Induced Closure of Marine Cloud Cells: Enhanced Effects in the Presence of Precipitation

Matthew W. Christensen[1], Peng Wu[1], Adam C. Varble[1], Heng Xiao[1], and Jerome D. Fast[1]

[1]Atmospheric Science & Global Change Division, Pacific Northwest National Laboratory, Richland, WA 99354, Washington, USA

Correspondence: Matthew W. Christensen (matt.christensen@pnnl.gov)

Abstract. The Weather Research Forecasting (WRF) V4.2 model is configured within a Lagrangian framework to quantify the impact of aerosols on evolving cloud fields. Simulations employing realistic meteorological boundary conditions are based on 10 case study days offering diverse meteorology during the Aerosol and Cloud Experiments in the Eastern North Atlantic (ACE-ENA). Cloud and aerosol retrievals in observations from aircraft measurements, ground-based Atmosphere Radiation
5 Measurement (ARM) data at Graciosa Island in the Azores, and A-Train and geostationary satellites are in good agreement with the simulations. Higher aerosol concentration leads to suppressed drizzle and increased cloud water content. These changes lead to larger radiative cooling rates at cloud top, enhanced vertical velocity variance, and increased vertical and horizontal wind speed near the base of the lower-tropospheric inversion. As a result, marine cloud cell area expands, narrowing the gap between shallow clouds and increasing cloud optical thickness, liquid water content, and the top-of-atmosphere outgoing shortwave flux.
10 While similar aerosol effects are observed in lightly to non-raining clouds, they tend to be smaller by comparison. These results show a strong link between cloud cell area expansion and the radiative adjustments caused by liquid water path and cloud fraction changes. These adjustments scale by 74% and 51%, respectively, relative to the Twomey effect. Given the limitations of traditional global climate model resolutions, addressing mesoscale cloud-state transitions at kilometer-scale resolutions or higher should be of utmost importance in accurately quantifying aerosol radiative forcing.

15 ## 1 Introduction

The surface temperature of Earth is kept cooler by the presence of low-level clouds, in particular stratocumulus. It has been estimated that a mere increase of about 4% in their global coverage would be enough to offset the radiative warming due to a doubling of atmospheric carbon dioxide (Randall et al., 1984). Aerosols, commonly emitted alongside greenhouse gases have the potential to decrease cloud droplet size and create more numerous cloud droplets that effectively suppress precipitation
20 and moisten the boundary layer (Albrecht, 1989). This process can increase the vertical and horizontal extents of cloud as well as their lifetime (Albrecht, 1989; Pincus and Baker, 1994; Bretherton et al., 2007; Christensen et al., 2020). However, an increase in aerosol concentration can also desiccate cloud through an increase in cloud-top entrainment caused by more effective evaporation in polluted clouds (Ackerman et al., 2004; Small et al., 2009) or through reduced cloud droplet sedimentation (Bretherton et al., 2007). These processes can even modify the cellular structure of clouds through changing cloud fraction

25   (Rosenfeld et al., 2006). However, the strength and sign of the cloud radiative effect depends on a multitude of meteorological factors such as lower troposphere stability and humidity, precipitation state (Chen et al., 2014), and time-scale for which clouds have been polluted (Wang and Feingold, 2009). These complex relationships result in poor understanding and large uncertainty in estimates of rapid cloud adjustments to changes in aerosol concentration (Bellouin et al., 2020), the so-called aerosol-cloud lifetime effect (Albrecht, 1989). It is critical to quantify and resolve process-scale cloud physics impacting rapid adjustments

30   in order to improve estimates of aerosol radiative forcing at global-scales (Seinfeld et al., 2016).

A preponderance of evidence linking aerosol and cloud radiative effects to the mesoscale structure of clouds has been growing in the literature over the past couple of decades (Rosenfeld et al., 2006; Wood, 2012; Christensen and Stephens, 2012; Eastman et al., 2021). Stratocumulus can exhibit cellular structures which appear closed or open with hexagonal-like or honeycomb shapes that organize on scales ranging from 10 – 50 km (Wood, 2005). The impact of aerosol on precipitation,

35   as proposed by (Rosenfeld et al., 2006), can reverse the direction of the wind flow through the vertical extent of the marine boundary layer, doubling cloud cover and converting cloud structure from open to closed cells. Eastman et al. (2021) observed that stronger surface winds and lower cloud droplet concentrations are typical prior to the transition of closed to open cells. Weather Research and Forecasting (WRF) model simulations from Zhou et al. (2018) indicate that moisture stratification and precipitation tend to increase horizontal cloud scales by enhancing updraft buoyancy via increased latent heating. Additionally,

40   longwave radiative cooling near cloud top plays a crucial role in increasing horizontal cloud scales, and sub-cloud moist cold pools tend to respond to, rather than determine, mesoscale variability. A Lagrangian framework has been shown to be effective in capturing upstream conditioning on developing clouds (Lewis et al., 2023) as well as to be used to quantify cloud lifetime, and track changes in cloud microphysics associated with changes in aerosol concentration and meteorological conditions (Christensen et al., 2020, 2023).

45   The shortwave cloud radiative effect of transforming open to closed stratocumulus cells was estimated to be as large as 109 W/m^2 in a composite of 50 case studies from MODIS observations from (Goren and Rosenfeld, 2014). Goren and Rosenfeld (2014) decomposed the aerosol indirect effect into the Twomey effect (the enhancement in shortwave cloud albedo caused by increasing cloud droplet concentration for fixed changes in liquid water path), and rapid adjustments containing liquid water path and cloud fraction changes. These were estimated to be approximately 26%, 32%, and 42%, respectively. Here,

50   we also quantify cloud water path and fraction adjustments but using a regression technique following Quaas et al. (2008) applied to kilometer-scale WRF model simulations of marine stratocumulus. We utilize a Lagrangian framework to capture the evolution of low-level clouds and examine how their cellular patterns change over time in order to answer the following research questions:

 – To what extent does a change in aerosol concentration modify the area and spacing between cloud cells?

55   – How does the aerosol indirect radiative effect vary over diverse meteorological conditions?

 – How does changing PBL and microphysics schemes affect the aerosol indirect effect?

 – How do liquid water path and cloud fraction adjustments compare to the Twomey effect?

To answer these questions we first describe the details of the data sets used in this study (section 2), set up several case study experiments in WRF that utilize a Lagrangian framework (section 3), and conclude with an assessment of the aerosol radiative forcing (sections 4 and 5).

2 Observational Data

The U.S. Department of Energy Atmosphere Radiation Measurement (ARM) program has been providing continuous measurements of cloud properties at Graciosa Island in the Azores for over a decade. This location is ideal for studying mesoscale structure (Jensen et al., 2021), turbulence (Ghate and Cadeddu, 2019), and aerosol-cloud interactions (Zheng et al., 2022b; Christensen et al., 2023; Varble et al., 2023) in marine stratocumulus clouds. Ground-based measurements from ARM, aircraft measurements from the Aerosol and Cloud Experiments in the Eastern North Atlantic (ACE-ENA; Wang et al., 2022), and satellite observations from geostationary and polar orbits are used to evaluate WRF simulations of boundary layer clouds passing over Graciosa Island.

Significant progress in the process-scale understanding of aerosol-cloud interactions, facilitated by observational data from Graciosa Island, reveals that the seasonal cycle plays a significant role in aerosol activation. During winter, when the clouds are more decoupled and connected to stronger updrafts compared to summertime conditions (Wang et al., 2022; Zheng et al., 2022a), a higher fraction of accumulation mode particles tends to be activated thereby resulting in decreasing the seasonal cycle in cloud droplet number concentration. Large eddy simulations (LES) using the WRF model with spectral bin microphysics and dynamical downscaling from a 19 km horizontal resolution to a 300 m grid spacing (Wang et al., 2020) demonstrated that imposing aerosol plumes at observed aircraft heights significantly reduces the effective droplet radius ($ACI_r = \frac{\partial \ln(r_e)}{\partial \ln(N_{CCN})} \approx -0.11$) and increases the liquid water path ($ACI_l \approx +0.14$). These cloud microphysical changes may modify the dynamics in the planetary boundary layer differently between seasons. Consequently, our work focuses on characterizing the cloud fraction response from numerous summer and winter case studies provided by ACE-ENA, conducting a deep investigation into mesoscale structural changes in clouds, and bridging the gap between cloud morphological changes and aerosol radiative forcing in low clouds.

2.1 Ground-based observations from ENA

Rain rate is retrieved from a laser optical OTT Particle Size and Velocity (PARSIVEL-2) disdrometer which measures the instantaneous rainfall rate of water flux from the number of drops in 32 size (0 to 25 mm) and 32 fall velocity bins (0.2 to 20 m/s) falling to the surface. The rain retrieval has a 6% absolute bias with respect to reference gauges over a 1-min sampling interval (Tokay et al., 2014) as provided in the LDQUANTS value added product (Hardin et al., 2020).

Cloud top height and low-level cloud fraction are estimated from the active remote sensing of clouds (ARSCL) product (O'Connor et al., 2004; Kollias et al., 2016; Clothiaux et al., 2001), which combines vertically pointing Ka-band radar and lidar data to produce high-resolution time-height cross sections of cloud boundaries.

Bottom of atmosphere shortwave and longwave radiative fluxes are provided by the ARM best-estimate cloud radiation dataset (ARMBECLDRAD; Xie et al., 2010; Tang and Xie, 2020) in hourly intervals using measurements from a infrared radiation station. Temperature and specific humidity profiles containing 266 altitude levels are provided every minute by the Interpolated Sounding (INTERPSONDE; Troyan, 2013) product that combines observations from radiosondes, the microwave radiometer (MWR), and surface meteorological instruments.

The effective radius of cloud droplets and optical depth in single-layer overcast liquid-only clouds is determined using the multifilter rotating shadowband radiometer (MFRSR) at a wavelength of 415 nm (Turner et al., 2021). The retrieval process relies on the algorithm developed by Min and Harrison (1996) for atmospheric radiative transfer. If the MWR successfully retrieves liquid water path, then the effective radius is calculated based on the MWR and MFRSR data. However, if such information is not available we exclude it (occurring less than 30% of cases) from the analysis to so that the results remain sensitive to variations in aerosol concentration as shown in Christensen et al. (2023).

2.2 ACE ENA Flights

The ARM Aerial Facility Gulfstream-159 (G-1) research aircraft flew from Terceira Island in the Azores during two intensive operational periods (IOPs) that occurred from June to July, 2017 and January to February, 2018 during ACE-ENA. Deployments during both seasons are used to evaluate the vertical profile of the bulk liquid water content measured by the multi-element water content system (WCM-2000; Matthews and Mei, 2017). The condensation particle counter (CPC) measures the number concentration of aerosols from 10 nm to 3 microns under-kinetic mode. Aerosol concentration uncertainties are approximately 15% (Fan and Pekour, 2018).

2.3 Satellite observations

Cloud-top effective droplet radius and cloud optical thickness are retrieved from the 1.6, 2.1, and 3.7-μm channels; cloud top temperature, pressure, and height are retrieved from longer-wavelength thermal channels on the Moderate Resolution Imaging Spectroradiometer (MODIS) instrument. These data are provided by the collection 6.1 cloud product (Platnick et al., 2017) at 1-km pixel-scale resolution at nadir from satellites Terra and Aqua, which pass over the region at approximately 10:30 am and 1:30 pm local time, respectively.

Imagery from the Geostationary Operational Environmental Satellite (GOES) Advanced Baseline Imager (ABI) of the National Oceanic and Atmospheric Administration (NOAA) GOES-R series satellite Pinker et al. (2022) is utilized to aid in visualizing the evolving characteristics of mesoscale cloud structures along Lagrangian trajectories. Full-disk images covering the entire region are made available every 15 minutes. These images have spatial resolutions of 0.5 km at nadir for the 0.64-μm visible channel and 2 km for the 3.9-μm and 11-μm channels.

The Clouds and the Earth's Radiant Energy System (CERES) Synoptic (SYN1deg-1Hour) edition 4.1 product (Rutan et al., 2015) provide similar cloud top retrievals to MODIS using similar algorithms (e.g. the MODIS collection 5 product) as well as top and bottom of atmosphere shortwave and longwave radiative fluxes that are gridded globally at $1 \times 1°$ every hour through

combining multi-spectral retrievals from a network of 16 geostationary satellites as well as the CERES instruments on Terra, Aqua, and Suomi National Polar-orbiting Partnership.

3 Methodology

Figure 1 depicts a 4-step procedure used to initialize and run the Weather Research and Forecasting (WRF) version 4.2 model
125 (Skamarock et al., 2021) in a Lagrangian framework. This technique uses an inner nest that moves through the WRF model (outer domain) at specified time-steps. First, the Hybrid Single-Particle Lagrangian Integrated Trajectory (HYSPLIT; Stein et al., 2015) version 5 model is used to calculate a 6-hour back and a 6-hour forward trajectory using the Modern-Era Retrospective analysis for Research and Applications, version 2 (MERRA-2; Gelaro et al., 2017) reanalysis meteorological data. Trajectories are calculated from the middle of the planetary boundary layer (determined in HYSPLIT). This height has been
130 shown to be representative for tracking the general flow of boundary layer clouds over the ocean (Christensen et al., 2020; Kazil et al., 2021; Christensen et al., 2023). Back trajectories are initialized at the Graciosa Island ARM site at 10 am local time before the Terra (morning at 10:30 am) and Aqua (afternoon at 1:30 pm) MODIS overpass times. Forward and backward trajectories are initialized at Graciosa Island and run for 6-hours. These trajectories are combined to form a 12-hour trajectory starting from the tail of the back trajectory and ending at the tail of the forward trajectory. This method ensures that the airmass
135 transits over the ARM site.

3.1 WRF Modeling

Nested simulations are performed using the WRF model (Figure 1 box 2). The outer (static) domain size is $12° \times 12°$ and is centered over the ARM site on Graciosa Island. The region is large enough to span the entire length of the back and forward Lagrangian trajectories. The outer domain has a horizontal grid spacing of 4 km and a vertical grid that is log-stretched where
140 the spacing is approximately 50 m near the surface and increases to 150 m throughout the PBL to the top of the model at 20 km. The model time-step is 10 s. The outer domain is used to characterize the large-scale meteorological flow and boundary conditions for the inner domain.

The inner domain allows for convection-permitting scales and moves along the HYSPLIT trajectory using the multi-incremental 4D-Var system which allows for translating (moving) nests within WRF (similar to vortex tracking for hurricanes
145 as described in Zhang et al., 2014). WRF was compiled using preset moves to permit higher spatial resolution simulations within the inner domain which is is computationally more efficient than high resolution across the entire outer domain. The inner domain translates in time (across the outer domain) according to the pre-computed locations using HYSPLIT. Given the spatial scales of typical cellular maritime cloud organization (30 to 40 km; Wood, 2005), the inner domain is spatially large enough to capture the largest scales of variability spanning approximately 200×300 km^2 with a horizontal grid-spacing that
150 is 5 times finer than the outer nest (800 m) with the same vertical resolution.

Boundary conditions are initialized and updated every 6 hours during simulation using reanalysis data from MERRA-2 which is spatially gridded at 0.5-degree resolution with 72 vertical levels and provided every 6 hours. We have tested WRF

using other meteorological data sets (details described in Text S1) and find that the choice of the reanalysis product does not significantly alter the results. To coincide with earlier work (Christensen et al., 2023) we use MERRA-2 to drive the WRF
155 boundary conditions for this study.

We use a 6-hour spin-up period to allow sufficient time for the cloud properties to reach steady state. After this period, the inner two-way nest begins to move within the WRF model according to the HYSPLIT trajectory computed using the same reanalysis product as that was used to drive the WRF model. The simulations are performed with the aerosol-aware Thompson bulk microphysical parameterization scheme (Thompson and Eidhammer, 2014) with explicit cloud droplet nucleation treat-
160 ment following Köhler activation theory. Look up tables generated from parcel modeling are used to provide the cloud droplet number concentration based on predicted temperature, vertical velocity, number of hygroscopic aerosol particles also referred to as 'number of water friendly aerosols' (NWFA), and predetermined values of hygroscopicity parameter and aerosol mean radius. Aerosol sensitivity experiments follow the same approach as described in Thompson and Eidhammer (2014) in which the input mass mixing ratio of each aerosol species (dust, sea salt, black and organic carbon, and sulfate aerosols) is obtained
165 from GOCART and is converted to NWFA concentration using assumed lognormal distributions with characteristic diameters and geometric standard deviations taken from Chin et al. (2002) (their Table 2). Next, we modify the NWFA concentration profile climatology averaged over 7 years using the following scale factors: 0.01 (pristine), 0.1 (clean), 1.0 (control), and 10.0 (polluted) for each experiment, respectively (Figure 1 box 3). Note, that no changes are made to the assumed aerosol chemical species composition, hygroscopicity parameter (0.4 in experiments performed in this research), and aerosol mean radius (0.04
170 μm). These scale factors significantly affect the NWFA concentration as shown in Figure S2. Lower condensation particle concentrations (CPC) in cloud-free air sampled by the aircraft suggest that the control simulation of NWFA may be more polluted than the observations on this particular day. However, the CPC and NWFA serves as a rough comparison as the characteristics (namely the size distribution and hygroscopicity) of these two quantities may differ. As discussed later, cloud droplet number concentrations are also affected by NWFA with median values broadly approaching 20, 50, 250, and 450 cm^{-3} for our pristine
175 (N1), clean (N2), control (N3), and polluted (N4) aerosol experiments, respectively.

The Level-3 Mellor-Yamada-Nakanishi-Niino (MYNN3) PBL scheme (Nakanishi and Niino, 2009) predicts TKE and other second-order moments within the PBL. The Rapid Radiative Transfer Model for GCMs (RRTMG) specifies the size of hydrometers and utilizes the correlated-k approach to calculate fluxes and heating rates accurately (Iacono et al., 2008) and efficiently through its use of a Monte-Carlo Independent Column Approximation technique (Pincus et al., 2003). The simulations utilize
180 the Noah land surface model (Barlage et al., 2010) as well as the Tiedtke cumulus scheme (Zhang et al., 2011).

Model evaluation (Figure 1 box 4) is carried out using output from the WRF-Solar model (Jimenez et al., 2016) which, when run online, passes the the effective radius of cloud particles from microphysics to radiation parameterizations (Thompson and Eidhammer, 2014) thereby affecting cloud albedo and permitting the quantification of the aerosol indirect effect (Thompson et al., 2016). WRF-Solar includes a solar diagnostics package that adds a number of two-dimensional variables output from
185 which we use cloud fraction, liquid effective droplet radius, optical thickness, and liquid water path (computed from the effective radius and optical thickness quantities, i.e. $LWP = \frac{2}{3}\tau_c R_e$, τ_c is the cloud optical thickness, and R_e is the effective

droplet radius; Stephens, 1978). These quantities (that are weighted towards the cloud top) have been shown to be comparable with MODIS observations (Otkin and Greenwald, 2008). A summary of the model setup is listed in Table 1.

3.2 Case Studies

190 Figure 2 shows our selected case studies. Days are selected based on the following criteria: 1) a dearth of high-level cloud over the trajectory for optimal comparison with satellite retrievals, 2) aircraft measurements coinciding with intensive operation periods (IOP) 1 (6/25/2017 - 7/25/2017) and 2 (2/1/2018 - 2/25/2018), and 3) diverse meteorological conditions to study the impacts of precipitation, atmospheric stability, and free-tropospheric humidity states on aerosol-cloud interactions. Across the experiments, the height of the PBL top varied from 600 m to 1710 m and the surface air temperature varied from $13 -$
195 $22°C$ as determined by meteorological soundings averaged over the entire day. Daily total accumulated precipitation from the disdrometer varied from 0 - 4 mm. A wide range of cloud patterns were observed including disorganized (small, isolated clouds or clouds with no discernible pattern), homogeneous (solid cloud deck with no discernible pattern), closed-cells (cells filled with cloud), open-cells (cells where the center is devoid of cloud). These classifications are broadly inferred using the definitions described in (Wood and Hartmann, 2006). Table 2 lists key quantities of interest for the cases displayed in Figure 2.
200 It is noteworthy to mention that while we aim to select cases which did not have ice cloud in the observations, the WRF model sometimes simulated them above the boundary layer (7/18/17) and within the boundary layer during two of the wintertime IOP case studies (1/24/18 and 1/25/18). Potential impacts of simulated ice cloud on the analysis are discussed in subsequent sections.

3.3 Lagrangian Framework and Dataset Integration

205 Figure 3 shows the evolution of shallow clouds in the Lagrangian trajectory for the lightly drizzling day of 7/18/2017. This case study forms the backbone for many of the inter-comparisons made throughout this work. Satellite retrievals from GOES and MODIS are aggregated over a $1 \times 1°$ region (yellow box) during each time-interval (15 minutes) along the trajectory. CERES gridded-data is interpolated in space and time to the same trajectory grid-box. WRF simulations at roughly km-scale are aggregated over the same region and timescale as the Lagrangian trajectory. Both the observations and simulations show
210 persistent closed cell clouds throughout the day. These clouds produce very light drizzle as indicated by the Ka-band radar (Fig. 2e) and disdrometer measurements at Graciosa Island (Table 2). An evident wake island effect is observed and simulated in the downstream region from the Azores. In general, the low-level flow and horizontal displacements of the clouds are well captured using the Lagrangian framework as depicted in Movie S1.

4 Results

215 In the first part of the analysis we quantify the effect of aerosol changes on the mesoscale structure of clouds (i.e. size and distance between cloud cells) and associated radiative impacts from an ensemble of 40 WRF simulations spanning 10 different case studies with 4 varying aerosol concentrations (a set of 4, for each case study day) offering diverse meteorology and

cloud types. This particular set of simulations uses MYNN3 and Thompson (aerosol-aware) PBL and microphysics schemes, respectively. In the second part, variations in the aerosol indirect effect from case study day 7/18 using different PBL and microphysical scheme choices across 26 WRF experiments is assessed and quantified.

4.1 Impact of aerosol on the mesoscale structure of clouds

Cloud objects are detected using the watershed technique, following the methodology described in Wu and Ovchinnikov (2022). Because the standard WRF model output does not include simulated channel reflectances for MODIS, comparisons are made based on the LWP. The only difference between Wu and Ovchinnikov (2022) and our study is that we use LWP instead of the MODIS reflectance. As LWP scales well with the visible cloud albedo (Stephens, 1978), the replacement of LWP for visible reflectance is suitable after thresholds have been linearly scaled. Moments of the LWP distributions have been used for cloud classification of marine stratocumulus in several studies (e.g., see Wood and Hartmann, 2006; Zheng et al., 2018). The segmentation procedure initially smooths the LWP field to remove random field variations while preserving object boundaries using a two-dimensional Gaussian filter with a kernel standard deviation of 250 g m^{-2}. Next, cloud objects are detected using a watershed technique. A centroid is assigned to each cloud object based on the distribution of cloudy pixels with LWP greater than 100 g m^{-2}. Cloud objects are formed if a common interface is shared. An edge weight is computed, and if the difference between adjacent pixels is greater than 4 g m^{-2} the two objects are merged and a new centroid is assigned to the object.

To determine the spacing between cloudy object centers, we compute the distance of each cloud object centroid to all other centroids and select the minimum distance (i.e., D_c). Due to variable sizes of the cloud objects, we also compute the distance of all edge pixels of an object to all of the edge pixels of all other objects and select the minimum distance (D_e). This latter method provides an estimate of the closest distance between neighboring cloud object boundaries, thus removing the effect of cloud fraction on distances between clouds that is not accounted for with cloud object centroids.

Cloud objects are identified in WRF (Fig. 4b) every 15 mins along the trajectory and in MODIS at the Terra and Aqua overpass times (Fig. 4d). Cloud area ranges from about 1 - 500 km^2 in WRF and MODIS (Fig. S3a). The majority are at scales less than about 10 km, a result similarly found in Wu and Ovchinnikov (2022) and (Wood and Hartmann, 2006), based on power spectral analysis of the spatial variance in LWP. The distance between cloud object centroids is similar between MODIS and WRF with a mean value of approximately 11 km and median value of roughly 5 km for this particular case study (Fig. S3b).

The size and spacing between cloud objects is to some extent dictated by the background aerosol concentration. Figure 5a and b shows that the average cell area and spacing between object centroids increases as the background aerosol concentration increases. The distance between cloud edges decreases as the aerosol concentration increases (Figure 5c). This is evident when comparing 'snapshots' of the pristine and polluted experiments taken at the same time (Fig. 5d-e). The cloud objects are spreading away from each other but they are also becoming larger and filling the gaps between clouds as aerosol loading increases.

To characterize uncertainty and determine whether this relationship is robust, a sensitivity test of the segmentation algorithm is performed over a range of minimum LWP thresholds for defining cloud object edges spanning 1 to 500 g m^{-2}. Figure S4

shows that the area of the cloud objects become larger with increasing aerosol concentration. This response is robust across the full range of LWP threshold values. The largest sensitivity of this relationship occurs around 200 g m^{-2}. This unique threshold LWP value is also a turning point for which further increases in LWP decrease the number of detected cloud objects, which impacts cell separation distance. Furthermore, the cloud fraction is larger under polluted conditions and this relationship is robust for each minimum LWP threshold value (Fig. S4d). As 100 g m^{-2} forms roughly the midpoint value we select this representative threshold for segmenting clouds in this analysis.

4.2 Aerosol-cloud interactions

Two case studies, one with lightly precipitating clouds and another with heavier precipitating clouds are examined in detail during the summertime IOP period for quantifying the effects of aerosol on precipitating and lightly-precipitating clouds.

4.2.1 Lightly-Precipitating clouds

On 7/18/17 closed-cell type clouds were found in the vicinity of the Azores. The clouds produced a light amount of precipitation where only approximately 0.02 mm was recorded in the distrometer measurements from ARM. Aircraft measurements of the cloud water content on this day fit within the range of variability simulated for clouds in the WRF model (Figure 6a). Cloud tops from the aircraft measurements imply that the WRF simulates a slightly deeper than observed boundary layer by approximately 200 m. We find reasonable agreement between MODIS, CERES, and ARM data sets with the WRF simulations (Fig. 7). Cloud optical depth and radiative fluxes tend to agree more closely with the clean and control WRF experiments. The agreement not being closest with the control experiment may be indicative of the following issues: 1) a bias in the climatological aerosol concentrations (being too high), 2) the Thompson scheme may be nucleating too many aerosols, or 3) scavenging rates are not large enough. Despite these differences, the chosen schemes resolve essential characteristics of a realistic boundary layer based on the reasonable agreement in the cloud relevant properties.

Rain water mixing ratio, also forming closer to cloud top in the cleaner experiments, decreases up to an order of magnitude as background aerosol concentration increases (Figure 6b). A modest increase in cloud water content and cloud water mixing ratio is found in the more polluted simulations throughout all levels in the cloud. This result is consistent with the indirect effect using the Thompson microphysics scheme described in Thompson and Eidhammer (2014). An increase in aerosol concentration also results in smaller cloud droplet effective radius (Fig. 7a), larger cloud optical thickness, larger liquid water path, and larger droplet concentration (Fig. 7b,c,d), cloud-top quantities obtained from WRF-Solar. The more polluted aerosol experiments with optically thicker clouds result in more reflected solar radiation at the top of the atmosphere and less incoming solar radiation at the bottom of the atmosphere despite having slightly lower cloud tops. The slightly elevated cloud tops in the more pristine simulation also have elevated cloud bases and are more decoupled from surface moisture. Nonetheless, all simulated cloud top heights are within the range of variability in the ARM and satellite observations.

Cloud properties tend to vary over the course of the trajectory with increasing cloud optical thickness, liquid water path, and cloud top height. This is accompanied by an increase in sea surface temperature and more unstable boundary layer conditions along with rising lifted condensation level and decreasing free tropospheric humidity (Fig. S5). A deepening boundary layer is

285 expected given the warming sea surface temperature (Eastman et al., 2016) but despite the changing meteorological conditions over the trajectories, the cloud changes related to changes in aerosol loading are systematic along the trajectories for a 12 hour period.

4.2.2 Precipitating clouds

In comparison to the previous case study, the boundary layer on 7/15 is about 750 m deeper and the accumulated rainfall is

290 significantly larger; 3.9 mm. Much like the previous light drizzle case study, the properties of precipitating clouds on 7/15/17 also broadly fit within the range of variability in cloud water content as measured by aircraft observations (Figure 8) and LWP by satellite and ARM retrievals (Fig. S6c). Simulated cloud top heights tend to be higher than the observations during the afternoon hours. Figure 2d shows that the clouds were much more vigorous as indicative by the relatively large radar reflectivities in the early morning and late afternoon periods outside of the trajectory period which could be responsible for the

295 mismatch in the simulated and actual cloud top heights. Nevertheless, peak cloud water contents in the control simulation are about 40% larger and peak rain water mixing ratios are about 90% larger on 7/15 (precipitating case study) compared to 7/18 (drizzling case study). Furthermore, the cloud water content increase due to increasing aerosol concentration is significantly larger on 7/15 compared to 7/18.

Simulations with elevated concentrations of aerosols have larger cloud top shortwave and longwave radiative cooling rates.

300 The net radiative cooling rate decreases from approximately -10 K/d in the clean simulations to -30 K/d in the more polluted simulations (Figure 9). Mean vertical and horizontal wind velocity near the cloud top also tends to be larger in the more polluted simulations. Vertical velocity variance and turbulence throughout the boundary layer tend to be larger in the more polluted simulations. Vertical profile shapes of these quantities are similar, albeit less in magnitude, for the light-drizzle simulations. Rainfall suppression in the more polluted simulations make the updrafts weaker in the lower planetary boundary

305 layer but stronger in the upper PBL where radiative cooling rates are larger. As a result, polluted clouds exhibit larger lateral displacements near the base of the inversion causing significant widening of the clouds and increase in cloud fraction.

Additional tests are carried out at 1 km horizontal grid spacing to determine the relative roles of cooling caused by rain drop evaporation (by setting the temperature and moisture tendencies caused by changes in rain mass evaporation in the Thompson microphysics scheme to zero), cloud radiative effect (setting icloud=0 in the namelist file), and the cumulus scheme (by turning

310 it off) on the results. Rain evaporation below cloud base stabilizes the atmosphere, producing decoupling and less turbulence (Wood, 2012). However, Fig. S7 shows that turning off rain droplet evaporation results in only a small relative change in cloud and rain mixing ratios, radiative cooling, and turbulence. Turning off the radiation to the clouds significantly decreases turbulent mixing, cloud top height, and rain water mixing ratio. Similarly, turning off the cumulus scheme significantly decreases cloud and rain water mixing ratio and radiative cooling rates.

315 Fig. S8 shows the outcome of these sensitivity experiments on the aerosol impact on cloud properties. In general, an increase in aerosol concentration enhances cloud fraction, liquid water path, and cloud area extent as aerosol loading increases. Turning off cloud interactions with radiation removes the effects of changes in cloud radiative heating and cooling, but clouds still expand (albeit less so) simply due to precipitation suppression by aerosols. This may indicate that low-clouds expand due

to precipitation suppression, through reducing the magnitude of the primary cloud sink; next changes in radiative effects
320 cause further increases in cloud fraction (approximately 100% more based on Fig. S8). This cloud radiative feedback suggests
an important contribution to promoting the initial cloud expansion via precipitation suppression by aerosol. For removal of
rain evaporation, the precipitation effect on PBL turbulence is turned off. While this no longer conserves energy (which is
unavoidable in such sensitivity tests) we continue to simulate strong cloud expansion due to increased aerosol concentration
and this is largely due to the suppression of precipitation and growth of the cloud.

325 ## 4.3 Aerosol-cloud interactions across 10 case studies

A suite of aerosol experiments spanning 10 case studies with varying meteorological conditions provides 40 WRF simulation
experiments to examine aerosol indirect radiative effect across a range of meteorological and cloud conditions. These case
studies are summarized in Table 2.

4.3.1 Aerosol indirect radiative effect

330 The aerosol indirect radiative effect is calculated from the change in the top of atmosphere outgoing shortwave flux caused by
a change in N_d and can be written as

$$RE_{aci} = -\overline{F^\downarrow}\phi_{atm}\frac{f_c\alpha_c(1-\alpha_c)}{3N_d}\left(1+\frac{5}{2}\frac{\Delta\ln L}{\Delta\ln N_d}+\frac{3(\alpha_c-\alpha_{clr})}{\alpha_c(1-\alpha_c)}\frac{\Delta\ln f_c}{\Delta\ln N_d}\right)\overline{\Delta N_d} \tag{1}$$

where, $F^\downarrow$ is the top of atmosphere (TOA) incoming solar radiation, ϕ_{atm} is the transfer function that accounts for the
average albedo of the non-cloudy air above the surface and takes an average value of 0.7 (Diamond et al., 2020), f_c is the cloud
335 cover fraction, α_c is the cloud albedo, N_d is the droplet concentration, L is the liquid water path, and α_{clr} is the clear-sky
albedo. The full derivation, based on Quaas et al. (2008) and Christensen et al. (2023), is described in Text S1.

Quantities in equation 1 are computed over each hourly interval over a $1° \times 1°$ domain moving along the trajectory. The Δ
symbols denote differences between aerosol experiments of varying aerosol concentrations (e.g. dirty - pristine, control - clean,
etc.). The $\overline{F^\downarrow}$ is the daily-mean solar insolation and $\overline{N_d}$ represents the difference between two aerosol experiments. A linear
340 least squares method is also used to compute $\frac{\Delta\ln L}{\Delta\ln N_d}$ and $\frac{\Delta\ln f_c}{\Delta\ln N_d}$ terms . On average, we find that the difference in methods
(difference between experiments vs using a fitted slope across all four experiments) varies by less than 15%. By using a wide
range of aerosol concentrations we capture the range of variability in ACI but acknowledge that non-linearity in the relationship
between cloud variables with N_d may be missed from the use of only 4 aerosol experiments.

Figure 10 shows the relationship of key variables as they change in response to increasing background aerosol concentrations
345 in the WRF model. In most cases, there is good agreement in the sign of the response across diverse case studies. An increase
in aerosol concentration enhances the top of atmosphere reflected sunlight, cloud fraction, liquid water path, cloud optical
thickness, and cloud object area. A robust decrease in droplet effective radius is also evident. While responses are mostly
consistent, the magnitude can vary substantially. Cases where significant precipitation occur (7/15 and 1/25) exhibit the largest
increases in liquid water path, cloud optical thickness, and cloud object area. Days having light rain (7/18, 7/6, 7/12) or no

350   measurable rain (6/30, 1/24) have significantly weaker responses by comparison. Figure 11a,b shows the effect of precipitation on the liquid water path and cloud fraction aerosol adjustments. While there is some scatter across experiments, this result generally agrees with Chen et al. (2014); an increase in aerosol concentration has a stronger radiative effect on precipitating clouds compared to non-precipitating clouds due to the suppression of precipitation causing cloud water to increase. While drizzle suppression reduces scavenging of cloud droplets and goes into spreading the cloud vertically, the horizontal spreading

355   of the clouds through increased cloud object area is highly significant.

The Twomey radiative effect is estimated as -57.9 $\pm$ 11.0 W m^{-2} with a range extending from -17.6 W m^{-2} to -107.5 W m^{-2} across these cases. This estimate is based on the local solar insolation, which at this location, can vary significantly between winter and summer IOP periods. Note, this estimate is the radiative effect, not the radiative forcing, and hence does not include the changes in aerosol concentration attributed to anthropogenic sources (i.e. the present-day minus pre-industrial values). The

360   radiative effect is estimated from aerosol experiments that have a wide range of aerosol concentrations (as shown in Fig. S1). The quantification of the sensitivity in the cloud radiative effect to changes in cloud droplet concentration are similar to those found in Goren and Rosenfeld (2014) or from local-scale aerosol perturbations found in ship tracks (Christensen and Stephens, 2012).

To make the results more intuitive, Table 3 lists the ratios of the liquid water path and cloud fraction adjustments scaled by

365   the Twomey effect. These enhancements range from 10 - 150 % for the LWP_{adj}; a result that is similar to that found across multiple GCM experiments in (Gryspeerdt et al., 2020) and the observations in Goren and Rosenfeld (2014). During both IOP periods we find that the largest indirect radiative effects tend to coincide with the largest daily precipitation rates (Figure 11c). These cases are also consistent with those which show the largest cell area growth as a function of aerosol loading (Figure 10). The cloud object area expansion relationship is not as strong during the wintertime IOP period, possibly because ice is

370   produced and can lead to glaciation indirect effects that can produce opposite precipitation responses compared to warm clouds (Lohmann, 2002; Christensen et al., 2014). Figure S9 shows that the fraction of liquid-to-ice is very high in the 1/24/18 and 1/25/18 cases. Thus, while some ice is simulated, the general tendencies for the Twomey and rapid adjustments, as well as the cloud morphological changes, remain consistent with the warm cloud responses (Figure 10). While aerosol effects on ice clouds are a key component to quantifying aerosol radiative forcing, it remains outside the scope of this study to examine it

375   further in this work.

4.3.2   Impact of changing PBL and microphysics schemes

We devise a set of sensitivity experiments where the microphysics and PBL schemes are varied to assess the uncertainty of modeling boundary layer clouds and ACI. These simulations use the double-moment Morrison microphysics (Morrison et al., 2005) scheme with fixed cloud droplet number concentration. For the Morrison scheme, we used fixed droplet number

380   concentrations with values of 20, 80, 320, and 1020 cm^{-3} for our pristine (N1), clean (N2), control (N3), and polluted (N4) aerosol experiments, respectively. Values for the more polluted runs were increased to coincide with the scale factors used in the Thompson (aerosol-aware) scheme for simulating similar values of the cloud droplet number concentrations. The additional PBL schemes for testing use the non-local Yonsei University (YSU; Hong et al., 2006) or local Mellor–Yamada–Janjic (MYJ;

Mellor and Yamada, 1982) closure flux models. These schemes have differences in vertical mixing strength which affect
385 entrainment of dry air from above the PBL and can impact cloud properties differently depending on the scheme chosen (Hu
et al., 2010). A summary of each sensitivity experiment is listed in Table 4.

Figure 12 shows a comparison of WRF simulated LWP with satellite observations from several different microphysics
and PBL schemes for the 7/18/2017 case study described in Figure 3. All schemes simulate boundary layer cloud in a similar
geographic region as that observed by satellites. However, some of the WRF schemes under-predict LWP and cloud top
390 heights, in particular the YSU and MYJ PBL schemes (as shown in Fig. S10) with respect to MODIS. The MYJ scheme tends to
produce smaller cloud cells containing much smaller liquid water paths compared to the YSU and MYNN3 schemes. In general,
most of the simulations reproduce the vertical profiles of temperature, humidity, wind speed, and wind direction compared to
ARM radiosonde measurements (Fig. S11) but with a slightly elevated capping inversion and dew point temperature. Overall,
we find the best agreement with the Thompson and MYNN3 PBL schemes regarding how close the cloud and atmospheric
395 state compare to the observations.

To test the impact of using different schemes in WRF on the aerosol indirect effect, four aerosol experiments are carried out
for each model configuration, yielding a total of 24 simulations to quantify the range of variability in aerosol indirect effect for
the case study occurring on 7/18/17. Due to computational constraints, we ran these simulations at a lower spatial resolution
(3 km grid spacing for the inner nest) using 99 vertical levels. Here we exclude cloud area changes in the analysis due to the
400 poorer ability of the model to simulate these structures at lower resolution and focus more on the microphysical changes across
these model configurations instead.

Figure S12 shows the aerosol perturbations of various cloud properties for each of the six configurations. Like before, all
simulations show that an increase in aerosol concentration results in an increase in the reflected solar radiation, a reduction
in cloud droplet effective radius, and an increase in cloud optical depth. The lower simulation resolutions produce similar
405 sensitivities compared to the higher resolution simulation runs. For example, $\Delta \ln \tau_c / \Delta N_d$ for the higher resolution run is
0.55 ± 0.12 and 0.48 ± 0.15 for the lower resolution run. It is noteworthy that the liquid water path and cloud thickness responses
are negative in some of the configurations; however, a t-test indicates that there is not a significant difference from zero. The
variations ($\sigma RE_{aci} = \frac{\sigma_{err}}{RE_{aci}}$, estimated from the standard error, σ_{err}, computed from the standard deviation normalized by the
square root of the 10 cases divided by the total indirect effect effect) across experiments is approximately $\pm$ 30%. Given this
410 range of variability in the indirect effect, we infer the microphysical cloud responses are robust across a wide range of possible
model configurations. Thus, variations larger than this level in analyses of the 10 case studies with the Thompson and MYNN
schemes are likely to be more related to meteorological and cloud state modulations as opposed to these particular chosen
WRF schemes.

5 Conclusions

415 We devised a series of realistic WRF simulations using boundary conditions from MERRA-2 reanalysis to simulate PBL
clouds as they pass over Graciosa Island in the Azores during the ACE-ENA field campaign. Kilometer-scale simulations

were carried out within an inner-nest that moves along the Lagrangian flow of the PBL, making higher resolution simulations computationally feasible for studying aerosol-cloud interactions. The Lagrangian framework allows for the analysis of an evolving cloud field over time, although, for relatively short-timescales like those used here the aerosol responses were roughly
420 consistent along the length of trajectories. Cloud water content, temperature, humidity, and wind profiles were in the range of acceptable uncertainty as determined by comparison with aircraft observations and radiosonde measurements from Graciosa Island. WRF-simulated cloud microphysical properties and radiative fluxes were generally in closer agreement to the clean (not control) experiments. This result suggests that the baseline NWFA concentration are biased high at Graciosa Island. With the exception of WRF simulating higher cloud tops during the afternoon compared to MODIS and ARM, the simulated cloud
425 and radiative properties in general tend to fit within the range of observed uncertainty.

With these simulations, we addressed the following research questions:

– **To what extent does a change in aerosol concentration modify the area and spacing between cloud cells?** An increase in aerosol concentration suppresses precipitation, causing liquid water content and liquid water path to increase throughout the PBL. Through applying the cloud segmentation watershed algorithm developed by Wu and Ovchinnikov
430 (2022) we find that cloud water mass is re-distributed through the PBL horizontally and in some cases vertically through the expansion of the clouds. This is accompanied by a decrease in clear skies between clouds. The suppression of drizzle through an increase in aerosol concentration results in more cloud water. The cloud top radiative cooling rates and turbulent eddies are increased in strength under polluted conditions. Larger vertical velocity variance and horizontal winds near the cloud tops was found in the simulations with more aerosol. Through this process, the additional water
435 (not lost through drizzle) in polluted clouds is re-distributed both vertically as well as horizontally. This results in the expansion of cloud cells.

– **How does the aerosol indirect radiative effect vary over diverse meteorological conditions?** The sign of the aerosol indirect radiative effect is robust across all case study days. They all exhibit liquid water path and cloud fraction increases with increasing aerosol concentration, a similar result also found in the WRF simulations of Zheng et al. (2022a). As
440 found in previous studies (e.g., Chen et al., 2014), the strength of the radiative effect is strongly tied to the occurrence of precipitation. We find that the cloud area expansion is greater in environments that support deeper boundary layers with heavier precipitation and the magnitude is generally smaller in case studies with less background precipitation.

– **How does changing PBL and microphysics schemes affect the aerosol indirect effect?** A set of six WRF configurations using three different PBL and two different microphysics schemes revealed robust cloud responses to changes in
445 aerosol concentration. The range of variability on total indirect effect across configurations was approximately 30%. We conclude that the choice of valid WRF schemes plays less of a role on the indirect effect (at least from these configurations for one case study) than the impact of precipitation on aerosol-cloud interactions where the variations are larger across the 10 case studies.

– **How do liquid water path and cloud fraction adjustments compare to the Twomey effect?** Aerosol radiative effects
450 were decomposed into contributions from the Twomey effect and liquid water path and cloud fraction adjustments.

The liquid water path and cloud fraction adjustments scale as 74% and 51% increases relative to the Twomey effect, respectively. These adjustments are larger than those found in prior observations (Goren and Rosenfeld, 2014) especially in the simulations where the daily mean precipitation is largest where an increase in aerosol can have a larger impact on drizzle suppression and cloud water path enhancement.

455 In all 10 case studies, LWP adjustments were consistently positive. This result remained consistent even when different PBL and microphysics schemes were employed. Despite the diversity in meteorological conditions, we were unable to simulate the negative LWP responses sometimes reported in LES studies, albeit using different boundary conditions (Ackerman et al., 2004; Seifert et al., 2015). Negative LWP responses have been documented in satellite observations of ship tracks (Christensen and Stephens, 2012) and more broadly in non-precipitating clouds, particularly in the presence of excessive dry air conditions

460 above the marine boundary layer (Chen et al., 2014). Our findings generally align with positive LWP responses. These are also identified in WRF LES simulations from the same region used in Wang et al. (2020). However, the lack of a negative LWP response in our study may be attributed to an underestimation of autoconversion, a tunable parameter that delays the formation of raindrops, resulting in the increase in LWP as N_d increases. Similarly, underestimating sedimentation and entrainment rates may lead to a less efficient removal of cloud and rainwater, contributing to an increase in LWP (Bretherton et al., 2007).

465 The impact of tunable parameters like these on cloud cell expansion due to increased aerosol concentration will be explored in subsequent research. It remains crucial to constrain such parameters based on observations (Suzuki and Stephens, 2009; Golaz et al., 2013; Christensen et al., 2023; Varble et al., 2023), where possible, to enhance our understanding of aerosol-cloud interactions and radiative forcing.

Overall, these results suggest that an increase in aerosol concentration may result in significantly more cooling than would

470 otherwise be predicted by the Twomey effect at the relatively short spatio-temporal-scales (300 km over 12 hours) considered here. We find generally that aerosols close stratocumulus cells, increase liquid water path, and cloud fraction. These relationships become enhanced in the presence of precipitation. Given the tight link between these radiative impacts and the nature of the mesoscale organization of clouds and its sensitivity to aerosol, it may be prudent to resolve these radiative effects in larger-scale models for improved assessments of climate change.

475 *Code and data availability.* All ARM and ACE-ENA products are available at https://www.arm.gov/data/. CERES SYN Ed4a 4 product is available at https://ceres.larc.nasa.gov. MODIS collection 6 products are available at https://earthdata.nasa.gov. MERRA-2 data were obtained from https://goldsmr4.gesdisc.eosdis.nasa.gov/data/MERRA-2/. HYSPLIT trajectory code is available at https://www.ready.noaa.gov/HYSPLIT.php. An archive of the WRF namelist.input and trajectory files for each case study day are provided at https://portal.nersc.gov/project/m1657/wrf_lagrangian_aci/ All data and code availability websites were last accessed on 10 October 2023.

480 *Video supplement.* Movies S1 related to this article is available in the supplementary materials.

Author contributions. MWC wrote the manuscript and developed the Lagrangian trajectory approach and analysis. PW guided the implementation of the cloud segmentation algorithm. Research and development ideas, as well as writing and editing, were contributed by PW, ACV, and JDF.

Competing interests. At least one of the (co-)authors is a member of the editorial board of Atmospheric Chemistry and Physics.

485 *Acknowledgements.* We would like to thank Yuwei Zhang for valuable feedback and assistance in compiling and running the WRF model. This research has been supported by the Atmospheric System Research (ASR) program as part of the US Department of Energy, Office of Science, Office of Biological and Environmental Research under Pacific Northwest National Laboratory (PNNL) project 57131. PNNL is operated for the US Department of Energy by Battelle Memorial Institute under contract DE-A06-76RLO 1830. Observations from the ENA site and ACE-ENA campaign are supported by the Atmospheric Radiation Measurement (ARM) Climate Research Facility.

490 **References**

Ackerman, A. S., Kirkpatrick, M. P., Stevens, D. E., and Toon, O. B.: The Impact of Humidity above Stratiform Clouds on Indirect Aerosol Climate Forcing, Nature, 432, 1014–1017, https://doi.org/10.1038/nature03174, 2004.

Albrecht, B. A.: Aerosols, Cloud Microphysics, and Fractional Cloudiness, Science, 245, 1227–1230, https://doi.org/10.1126/science.245.4923.1227, 1989.

495 Barlage, M., Chen, F., Tewari, M., Ikeda, K., Gochis, D., Dudhia, J., Rasmussen, R., Livneh, B., Ek, M., and Mitchell, K.: Noah land surface model modifications to improve snowpack prediction in the Colorado Rocky Mountains, Journal of Geophysical Research: Atmospheres, 115, https://doi.org/https://doi.org/10.1029/2009JD013470, 2010.

Bellouin, N., Quaas, J., Gryspeerdt, E., Kinne, S., Stier, P., Watson-Parris, D., Boucher, O., Carslaw, K. S., Christensen, M., Daniau, A.-L., Dufresne, J.-L., Feingold, G., Fiedler, S., Forster, P., Gettelman, A., Haywood, J. M., Lohmann, U., Malavelle, F., Mauritsen, T.,
500 McCoy, D. T., Myhre, G., Mülmenstädt, J., Neubauer, D., Possner, A., Rugenstein, M., Sato, Y., Schulz, M., Schwartz, S. E., Sourdeval, O., Storelvmo, T., Toll, V., Winker, D., and Stevens, B.: Bounding Global Aerosol Radiative Forcing of Climate Change, Reviews of Geophysics, 58, e2019RG000 660, https://doi.org/10.1029/2019RG000660, 2020.

Bretherton, C. S., Blossey, P. N., and Uchida, J.: Cloud Droplet Sedimentation, Entrainment Efficiency, and Subtropical Stratocumulus Albedo, Geophysical Research Letters, 34, https://doi.org/10.1029/2006gl027648, 2007.

505 Chen, Y.-C., Christensen, M. W., Stephens, G. L., and Seinfeld, J. H.: Satellite-Based Estimate of Global Aerosol-Cloud Radiative Forcing by Marine Warm Clouds, Nature Geoscience, 7, 643–646, https://doi.org/10.1038/ngeo2214, 2014.

Chin, M., Ginoux, P., Kinne, S., Torres, O., Holben, B. N., Duncan, B. N., Martin, R. V., Logan, J. A., Higurashi, A., and Nakajima, T.: Tropospheric aerosol optical thickness from the GOCART model and comparisons with satellite and Sun photometer measurements, Journal of the Atmospheric Sciences, 59, 461–483, https://doi.org/Doi 10.1175/1520-0469(2002)059<0461:Taotft>2.0.Co;2, 2002.

510 Christensen, M. W. and Stephens, G. L.: Microphysical and Macrophysical Responses of Marine Stratocumulus Polluted by Underlying Ships: 2. Impacts of Haze on Precipitating Clouds, Journal of Geophysical Research: Atmospheres, 117, https://doi.org/10.1029/2011JD017125, 2012.

Christensen, M. W., Suzuki, K., Zambri, B., and Stephens, G. L.: Ship Track Observations of a Reduced Shortwave Aerosol Indirect Effect in Mixed-Phase Clouds, Geophysical Research Letters, 41, 6970–6977, https://doi.org/10.1002/2014GL061320, 2014.

515 Christensen, M. W., Jones, W. K., and Stier, P.: Aerosols Enhance Cloud Lifetime and Brightness along the Stratus-to-Cumulus Transition, Proc Natl Acad Sci U S A, https://doi.org/10.1073/pnas.1921231117, 2020.

Christensen, M. W., Ma, P.-L., Wu, P., Varble, A. C., Mülmenstädt, J., and Fast, J. D.: Evaluation of aerosol–cloud interactions in E3SM using a Lagrangian framework, Atmospheric Chemistry and Physics, 23, 2789–2812, https://doi.org/10.5194/acp-23-2789-2023, 2023.

Clothiaux, E. E., Miller, M. A., Perez, R. C., Turner, D. D., Moran, K. P., Martner, B. E., Ackerman, T. P., Mace, G. G., Marchand, R. T.,
520 Widener, K. B., Rodriguez, D. J., Uttal, T., Mather, J. H., Flynn, C. J., Gaustad, K. L., and Ermold, B.: The ARM Millimeter Wave Cloud Radars (MMCRs) and the Active Remote Sensing of Clouds (ARSCL) Value Added Product (VAP), NA, https://doi.org/10.2172/1808567, 2001.

Diamond, M. S., Director, H. M., Eastman, R., Possner, A., and Wood, R.: Substantial Cloud Brightening From Shipping in Subtropical Low Clouds, AGU Advances, 1, e2019AV000 111, https://doi.org/10.1029/2019AV000111, 2020.

525 Eastman, R., Wood, R., and Bretherton, C. S.: Time Scales of Clouds and Cloud-Controlling Variables in Subtropical Stratocumulus from a Lagrangian Perspective, Journal of the Atmospheric Sciences, 73, 3079–3091, https://doi.org/10.1175/JAS-D-16-0050.1, 2016.

Eastman, R., Terai, C. R., Grosvenor, D. P., and Wood, R.: Evaluating the Lagrangian Evolution of Subtropical Low Clouds in GCMs Using Observations: Mean Evolution, Time Scales, and Responses to Predictors, Journal of the Atmospheric Sciences, 78, 353 – 372, https://doi.org/https://doi.org/10.1175/JAS-D-20-0178.1, 2021.

530 Fan, M. and Pekour, M.: CPC_ACEENA, https://doi.org/10.5439/1440985, 2018.

Gelaro, R., McCarty, W., Suarez, M. J., Todling, R., Molod, A., Takacs, L., Randles, C. A., Darmenov, A., Bosilovich, M. G., Reichle, R., Wargan, K., Coy, L., Cullather, R., Draper, C., Akella, S., Buchard, V., Conaty, A., da Silva, A. M., Gu, W., Kim, G. K., Koster, R., Lucchesi, R., Merkova, D., Nielsen, J. E., Partyka, G., Pawson, S., Putman, W., Rienecker, M., Schubert, S. D., Sienkiewicz, M., and Zhao, B.: The Modern-Era Retrospective Analysis for Research and Applications, Version 2 (MERRA-2), Journal of Climate, 30, 5419–5454,

535 https://doi.org/10.1175/Jcli-D-16-0758.1, 2017.

Ghate, V. P. and Cadeddu, M. P.: Drizzle and Turbulence Below Closed Cellular Marine Stratocumulus Clouds, Journal of Geophysical Research-Atmospheres, 124, 5724–5737, https://doi.org/10.1029/2018jd030141, 2019.

Golaz, J.-C., Horowitz, L. W., and Levy, H.: Cloud tuning in a coupled climate model: Impact on 20th century warming, Geophysical Research Letters, 40, 2246–2251, https://doi.org/10.1002/grl.50232, 2013.

540 Goren, T. and Rosenfeld, D.: Decomposing aerosol cloud radiative effects into cloud cover, liquid water path and Twomey components in marine stratocumulus, Atmospheric Research, 138, 378 – 393, https://doi.org/https://doi.org/10.1016/j.atmosres.2013.12.008, 2014.

Gryspeerdt, E., Mülmenstädt, J., Gettelman, A., Malavelle, F. F., Morrison, H., Neubauer, D., Partridge, D. G., Stier, P., Takemura, T., Wang, H., Wang, M., and Zhang, K.: Surprising similarities in model and observational aerosol radiative forcing estimates, Atmospheric Chemistry and Physics, 20, 613–623, https://doi.org/10.5194/acp-20-613-2020, 2020.

545 Hardin, J., Giangrande, S. E., and Zhou, A.: Laser Disdrometer Quantities (LDQUANTS) and Video Disdrometer Quantities (VDIS-QUANTS) Value-Added Products Report, https://doi.org/10.2172/1808573, 2020.

Hong, S. Y., Noh, Y., and Dudhia, J.: A new vertical diffusion package with an explicit treatment of entrainment processes, Monthly Weather Review, 134, 2318–2341, https://doi.org/Doi 10.1175/Mwr3199.1, 2006.

Hu, X.-M., Nielsen-Gammon, J. W., and Zhang, F.: Evaluation of Three Planetary Boundary Layer Schemes in the WRF Model, Journal of

550 Applied Meteorology and Climatology, 49, 1831 – 1844, https://doi.org/https://doi.org/10.1175/2010JAMC2432.1, 2010.

Iacono, M. J., Delamere, J. S., Mlawer, E. J., Shephard, M. W., Clough, S. A., and Collins, W. D.: Radiative forcing by long-lived greenhouse gases: Calculations with the AER radiative transfer models, Journal of Geophysical Research: Atmospheres, 113, https://doi.org/https://doi.org/10.1029/2008JD009944, 2008.

Jensen, M. P., Ghate, V. P., Wang, D., Apoznanski, D. K., Bartholomew, M. J., Giangrande, S. E., Johnson, K. L., and Thieman, M. M.:

555 Contrasting characteristics of open- and closed-cellular stratocumulus cloud in the eastern North Atlantic, Atmospheric Chemistry and Physics, 21, 14 557–14 571, https://doi.org/10.5194/acp-21-14557-2021, 2021.

Jimenez, P. A., Hacker, J. P., Dudhia, J., Haupt, S. E., Ruiz-Arias, J. A., Gueymard, C. A., Thompson, G., Eidhammer, T., and Deng, A.: WRF-Solar: Description and Clear-Sky Assessment of an Augmented NWP Model for Solar Power Prediction, Bulletin of the American Meteorological Society, 97, 1249 – 1264, https://doi.org/10.1175/BAMS-D-14-00279.1, 2016.

560 Kazil, J., Christensen, M. W., Abel, S. J., Yamaguchi, T., and Feingold, G.: Realism of Lagrangian Large Eddy Simulations Driven by Reanalysis Meteorology: Tracking a Pocket of Open Cells Under a Biomass Burning Aerosol Layer, Journal of Advances in Modeling Earth Systems, 13, e2021MS002 664, https://doi.org/https://doi.org/10.1029/2021MS002664, e2021MS002664 2021MS002664, 2021.

Kollias, P., Clothiaux, E. E., Ackerman, T. P., Albrecht, B. A., Widener, K. B., Moran, K. P., Luke, E. P., Johnson, K. L., Bharadwaj, N., Mead, J. B., Miller, M. A., Verlinde, J., Marchand, R. T., and Mace, G. G.: Development and Applications of ARM Millimeter-Wavelength
565   Cloud Radars, Meteorological Monographs, 57, 17.1 – 17.19, https://doi.org/10.1175/AMSMONOGRAPHS-D-15-0037.1, 2016.

Lewis, H., Bellon, G., and Dinh, T.: Upstream Large-Scale Control of Subtropical Low-Cloud Climatology, Journal of Climate, 36, 3289 – 3303, https://doi.org/https://doi.org/10.1175/JCLI-D-22-0676.1, 2023.

Lohmann, U.: A glaciation indirect aerosol effect caused by soot aerosols, Geophysical Research Letters, 29, 11–1–11–4, https://doi.org/https://doi.org/10.1029/2001GL014357, 2002.

570   Matthews, A. and Mei, F.: WCM water content for ACE-ENA, https://doi.org/10.5439/1465759, united States, 2017.

Mellor, G. L. and Yamada, T.: Development of a Turbulence Closure-Model for Geophysical Fluid Problems, Reviews of Geophysics, 20, 851–875, https://doi.org/DOI 10.1029/RG020i004p00851, 1982.

Min, Q. and Harrison, L. C.: Cloud properties derived from surface MFRSR measurements and comparison with GOES results at the ARM SGP Site, Geophysical Research Letters, 23, 1641–1644, https://doi.org/https://doi.org/10.1029/96GL01488, 1996.

575   Morrison, H., Curry, J. A., and Khvorostyanov, V. I.: A New Double-Moment Microphysics Parameterization for Application in Cloud and Climate Models. Part I: Description, Journal of the Atmospheric Sciences, 62, 1665 – 1677, https://doi.org/https://doi.org/10.1175/JAS3446.1, 2005.

Nakanishi, M. and Niino, H.: Development of an Improved Turbulence Closure Model for the Atmospheric Boundary Layer, Journal of the Meteorological Society of Japan, 87, 895–912, https://doi.org/10.2151/jmsj.87.895, 2009.

580   O'Connor, E. J., Illingworth, A. J., and Hogan, R. J.: A Technique for Autocalibration of Cloud Lidar, Journal of Atmospheric and Oceanic Technology, 21, 777 – 786, https://doi.org/10.1175/1520-0426(2004)021<0777:ATFAOC>2.0.CO;2, 2004.

Otkin, J. A. and Greenwald, T. J.: Comparison of WRF Model-Simulated and MODIS-Derived Cloud Data, Monthly Weather Review, 136, 1957 – 1970, https://doi.org/10.1175/2007MWR2293.1, 2008.

Pincus, R. and Baker, M. B.: Effect of precipitation on the albedo susceptibility of clouds in the marine boundary layer, Nature, 372, 250–252,
585   1994.

Pincus, R., Barker, H. W., and Morcrette, J.-J.: A fast, flexible, approximate technique for computing radiative transfer in inhomogeneous cloud fields, Journal of Geophysical Research: Atmospheres, 108, https://doi.org/https://doi.org/10.1029/2002JD003322, 2003.

Pinker, R. T., Ma, Y. T., Chen, W., Laszlo, I., Liu, H. Q., Kim, H. Y., and Daniels, J.: Top-of-the-atmosphere reflected shortwave radiative fluxes from GOES-R, Atmospheric Measurement Techniques, 15, 5077–5094, https://doi.org/10.5194/amt-15-5077-2022, 2022.

590   Platnick, S., Meyer, K. G., King, M. D., Wind, G., Amarasinghe, N., Marchant, B., Arnold, G. T., Zhang, Z., Hubanks, P. A., Holz, R. E., Yang, P., Ridgway, W. L., and Riedi, J.: The MODIS Cloud Optical and Microphysical Products: Collection 6 Updates and Examples From Terra and Aqua, IEEE Transact. Geosci. Remote Sens., 55, 502–525, https://doi.org/10.1109/TGRS.2016.2610522, 2017.

Quaas, J., Boucher, O., Bellouin, N., and Kinne, S.: Satellite-based estimate of the direct and indirect aerosol climate forcing, Journal of Geophysical Research: Atmospheres, 113, https://doi.org/10.1029/2007JD008962, 2008.

595   Randall, D. A., J. A. Coakley Jr., Fairall, C. W., Kropfli, R. A., and Lenschow, D. H.: Outlook for research on subtropical marine stratiform clouds, Bull. Amer. Meteor. Soc., 65, 1290–1301, 1984.

Rosenfeld, D., Kaufman, Y. J., and Koren, I.: Switching cloud cover and dynamical regimes from open to closed Benard cells in response to the suppression of precipitation by aerosols, Atmospheric Chemistry and Physics, 6, 2503–2511, https://doi.org/10.5194/acp-6-2503-2006, 2006.

600   Rutan, D. A., Kato, S., Doelling, D. R., Rose, F. G., Nguyen, L. T., Caldwell, T. E., and Loeb, N. G.: CERES Synoptic Product: Methodology and Validation of Surface Radiant Flux, Journal of Atmospheric and Oceanic Technology, 32, 1121–1143, https://doi.org/10.1175/JTECH-D-14-00165.1, 2015.

Seifert, A., Heus, T., Pincus, R., and Stevens, B.: Large-Eddy Simulation of the Transient and near-Equilibrium Behavior of Precipitating Shallow Convection, Journal of Advances in Modeling Earth Systems, 7, 1918–1937, https://doi.org/10.1002/2015ms000489, 2015.

605   Seinfeld, J. H., Bretherton, C., Carslaw, K. S., Coe, H., DeMott, P. J., Dunlea, E. J., Feingold, G., Ghan, S., Guenther, A. B., Kahn, R., Kraucunas, I., Kreidenweis, S. M., Molina, M. J., Nenes, A., Penner, J. E., Prather, K. A., Ramanathan, V., Ramaswamy, V., Rasch, P. J., Ravishankara, A. R., Rosenfeld, D., Stephens, G., and Wood, R.: Improving our fundamental understanding of the role of aerosol-cloud interactions in the climate system, Proceedings of the National Academy of Sciences, 113, 5781–5790, https://doi.org/10.1073/pnas.1514043113, 2016.

610   Skamarock, W. C., Klemp, J. B., Dudhia, J., Gill, D. O., Liu, Z., Berner, J., Wang, W., Powers, J. G., Duda, M. G., Barker, D., and Huang, X.: A Description of the Advanced Research WRF Model Version 4.3 (No. NCAR/TN-556+STR), https://doi.org/doi:10.5065/1dfh-6p97, 2021.

Small, J. D., Chuang, P. Y., Feingold, G., and Jiang, H.: Can aerosol decrease cloud lifetime?, Geophysical Research Letters, 36, https://doi.org/10.1029/2009GL038888, 2009.

615   Stein, A. F., Draxler, R. R., Rolph, G. D., Stunder, B. J. B., Cohen, M. D., and Ngan, F.: NOAA's HYSPLIT Atmospheric Transport and Dispersion Modeling System, Bulletin of the American Meteorological Society, 96, 2059 – 2077, https://doi.org/https://doi.org/10.1175/BAMS-D-14-00110.1, 2015.

Stephens, G. L.: Radiation profiles in extended water clouds. II: Parameterization schemes, Journal of the Atmospheric Sciences, 35, 2123–2132, 1978.

620   Suzuki, K. and Stephens, G. L.: Relationship between radar reflectivity and the time scale of warm rain formation in a global cloud-resolving model, Atmos. Res., 12.010, doi:10.1016/j.atmosres., 2009.

Tang, S. and Xie, S.: Atmospheric Radiation Measurement (ARM) user facility, 2020: ARM Best Estimate Cloud Radiation (ARMBE-CLDRAD). 2014-01-01 to 2020-12-31, Eastern North Atlantic (ENA) Graciosa Island, Azores, Portugal (C1)., doi:10.5439/1333228., data set accessed 2022-01-19 at doi:10.5439/1333228., 2020.

625   Thompson, G. and Eidhammer, T.: A Study of Aerosol Impacts on Clouds and Precipitation Development in a Large Winter Cyclone, Journal of the Atmospheric Sciences, 71, 3636 – 3658, https://doi.org/10.1175/JAS-D-13-0305.1, 2014.

Thompson, G., Tewari, M., Ikeda, K., Tessendorf, S., Weeks, C., Otkin, J., and Kong, F.: Explicitly-coupled cloud physics and radiation parameterizations and subsequent evaluation in WRF high-resolution convective forecasts, Atmospheric Research, 168, 92–104, https://doi.org/https://doi.org/10.1016/j.atmosres.2015.09.005, 2016.

630   Tokay, A., Wolff, D. B., and Petersen, W. A.: Evaluation of the New Version of the Laser-Optical Disdrometer, OTT Parsivel2, Journal of Atmospheric and Oceanic Technology, 31, 1276 – 1288, https://doi.org/10.1175/JTECH-D-13-00174.1, 2014.

Troyan, D.: Interpolated Sounding Value-Added Product, https://doi.org/10.2172/1226794, 2013.

Turner, D., Q, C. L., Zhang, M. D., and Gaustad, K.: Atmospheric Radiation Measurement (ARM) user facility, 2021: Cloud Optical Properties from the Multifilter Shadowband Radiometer (MFRSRCLDOD): An ARM Value-Added Product. 2014-06-01 to 2019-10-27, Eastern

635   North Atlantic (ENA) Graciosa Island, Azores, Portugal (C1)., https://www.arm.gov/capabilities/vaps/mfrsrcldod, data set accessed 2022-01-19 at https://www.arm.gov/capabilities/vaps/mfrsrcldod, 2021.

Varble, A. C., Ma, P.-L., Christensen, M. W., Mülmenstädt, J., Tang, S., and Fast, J.: Evaluation of Liquid Cloud Albedo Susceptibility in E3SM Using Coupled Eastern North Atlantic Surface and Satellite Retrievals, EGUsphere, 2023, 1–39, https://doi.org/10.5194/egusphere-2023-998, 2023.

640 Wang, H. and Feingold, G.: Modeling mesoscale cellular structures and drizzle in marine stratocumulus. Part II: The microphysics and dynamics of the boundary region between open and closed cells, Journal of the Atmospheric Sciences, 66, 3257–3275, doi:10.1175/2009JAS3120.1, 2009.

Wang, J., Wood, R., Jensen, M. P., Chiu, J. C., Liu, Y., Lamer, K., Desai, N., Giangrande, S. E., Knopf, D. A., Kollias, P., Laskin, A., Liu, X., Lu, C., Mechem, D., Mei, F., Starzec, M., Tomlinson, J., Wang, Y., Yum, S. S., Zheng, G., Aiken, A. C., Azevedo, E. B., Blanchard, Y.,

645 China, S., Dong, X., Gallo, F., Gao, S., Ghate, V. P., Glienke, S., Goldberger, L., Hardin, J. C., Kuang, C., Luke, E. P., Matthews, A. A., Miller, M. A., Moffet, R., Pekour, M., Schmid, B., Sedlacek, A. J., Shaw, R. A., Shilling, J. E., Sullivan, A., Suski, K., Veghte, D. P., Weber, R., Wyant, M., Yeom, J., Zawadowicz, M., and Zhang, Z.: Aerosol and Cloud Experiments in the Eastern North Atlantic (ACE-ENA), Bulletin of the American Meteorological Society, 103, E619 – E641, https://doi.org/https://doi.org/10.1175/BAMS-D-19-0220.1, 2022.

Wang, Y., Zheng, X. J., Dong, X. Q., Xi, B. K., Wu, P., Logan, T., and Yung, Y. L.: Impacts of long-range transport of aerosols on marine-

650 boundary-layer clouds in the eastern North Atlantic, Atmospheric Chemistry and Physics, 20, 14 741–14 755, https://doi.org/10.5194/acp-20-14741-2020, 2020.

Wood, R.: Drizzle in Stratiform Boundary Layer Clouds. Part I: Vertical and Horizontal Structure, Journal of the Atmospheric Sciences, 62, 3011–3033, doi:10.1175/JAS3529.1, 2005.

Wood, R.: Stratocumulus Clouds, Mon. Wea. Rev., 140, 2373?2423, 2012.

655 Wood, R. and Hartmann, D. L.: Spatial variability of liquid water path in marine low cloud: the importance of mesoscale cellular convection, Journal of Climate, 19, 1748–1764, doi: 10.1175/JCLI3702.1, 2006.

Wu, P. and Ovchinnikov, M.: Cloud Morphology Evolution in Arctic Cold-Air Outbreak: Two Cases During COMBLE Period, Journal of Geophysical Research: Atmospheres, 127, e2021JD035 966, https://doi.org/https://doi.org/10.1029/2021JD035966, e2021JD035966 2021JD035966, 2022.

660 Xie, S., McCoy, R. B., Klein, S. A., Cederwall, R. T., Wiscombe, W. J., Jensen, M. P., Johnson, K. L., Clothiaux, E. E., Gaustad, K. L., Long, C. N., Mather, J. H., McFarlane, S. A., Shi, Y., Golaz, J.-C., Lin, Y., Hall, S. D., McCord, R. A., Palanisamy, G., and Turner, D. D.: CLOUDS AND MORE: ARM Climate Modeling Best Estimate Data: A New Data Product for Climate Studies, Bulletin of the American Meteorological Society, 91, 13 – 20, https://doi.org/10.1175/2009BAMS2891.1, 2010.

Zhang, C. X., Wang, Y. Q., and Hamilton, K.: Improved Representation of Boundary Layer Clouds over the Southeast Pacific in ARW-WRF

665 Using a Modified Tiedtke Cumulus Parameterization Scheme, Monthly Weather Review, 139, 3489–3513, https://doi.org/10.1175/Mwr-D-10-05091.1, 2011.

Zhang, X., Huang, X.-Y., Liu, J., Poterjoy, J., Weng, Y., Zhang, F., and Wang, H.: Development of an Efficient Regional Four-Dimensional Variational Data Assimilation System for WRF, Journal of Atmospheric and Oceanic Technology, 31, 2777 – 2794, https://doi.org/10.1175/JTECH-D-13-00076.1, 2014.

670 Zheng, X. J., Dong, X. Q., Ward, D. M., Xi, B. K., Wu, P., and Wang, Y.: Aerosol-Cloud-Precipitation Interactions in a Closed-cell and Non-homogenous MBL Stratocumulus Cloud, Advances in Atmospheric Sciences, 39, 2107–2123, https://doi.org/10.1007/s00376-022-2013-6, 2022a.

Zheng, X. J., Xi, B. K., Dong, X. Q., Wu, P., Logan, T., and Wang, Y.: Environmental effects on aerosol-cloud interaction in non-precipitating marine boundary layer (MBL) clouds over the eastern North Atlantic, Atmospheric Chemistry and Physics, 22, 335–354, https://doi.org/10.5194/acp-22-335-2022, 2022b.

675 Zheng, Y., Rosenfeld, D., and Li, Z.: Estimating the Decoupling Degree of Subtropical Marine Stratocumulus Decks From Satellite, Geophysical Research Letters, 45, 12,560–12,568, https://doi.org/https://doi.org/10.1029/2018GL078382, 2018.

Zhou, X., Ackerman, A. S., Fridlind, A. M., and Kollias, P.: Simulation of Mesoscale Cellular Convection in Marine Stratocumulus. Part I: Drizzling Conditions, Journal of the Atmospheric Sciences, 75, 257 – 274, https://doi.org/https://doi.org/10.1175/JAS-D-17-0070.1, 2018.

HYSPLIT

Step 1: Compute Trajectory
- Parcel trajectory
- 6-hour backward and forward trajectory
- Initialized in middle of PBL
- MERRA2 reanalysis

WRF

Step 2: Feed trajectory into WRF model
- Compile with preset moves
- Inner domain nest moves along HYSPLIT trajectory

Model

Step 3: Run aerosol experiments
N1: Pristine (0.05)   N2: Clean (0.1),
N3: Control (1.0)   N4: Polluted (10.0)

Evaluate

Step 4: Evaluate Model
- Compare WRF-Solar optical properties with satellite and ACE ENA flight data.
- Compute aerosol radiative effect.

Figure 1. Flow chart showing the methodology of implementing the Lagrangian framework for studying aerosol-cloud interactions in the WRF model.
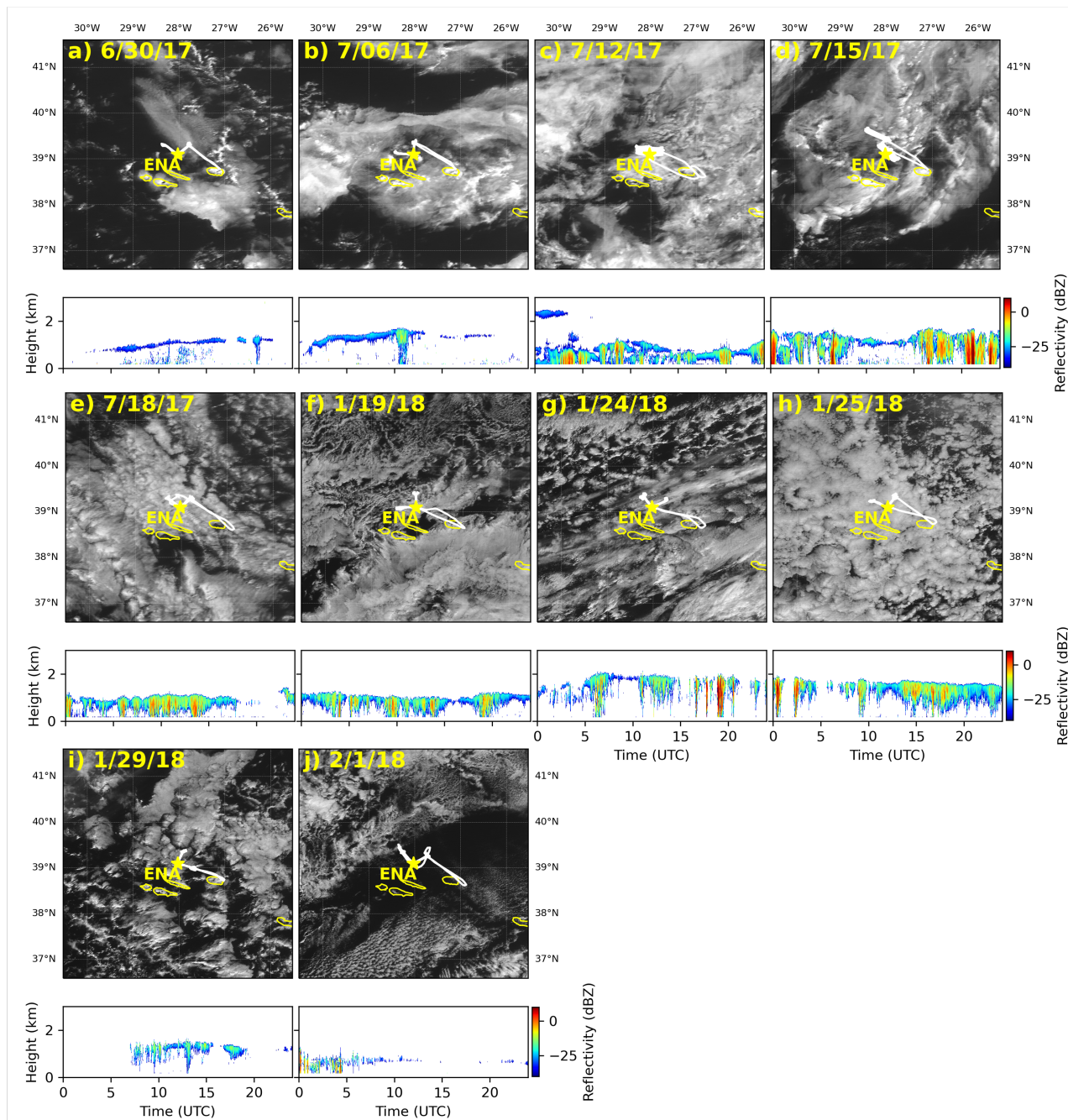
Figure 2. Case studies during summer (a - e) and winter (f - j) ACE-ENA IOP periods. Panels display GOES visible images at 13:00 UTC displayed over 4 × 4 ° regions centered over Graciosa Island (yellow star denotes the ARM site). Aircraft flight positions are shown as white lines. Vertically pointing Ka-band reflectivity at the ARM site is displayed over a 24-hr period for the corresponding days.
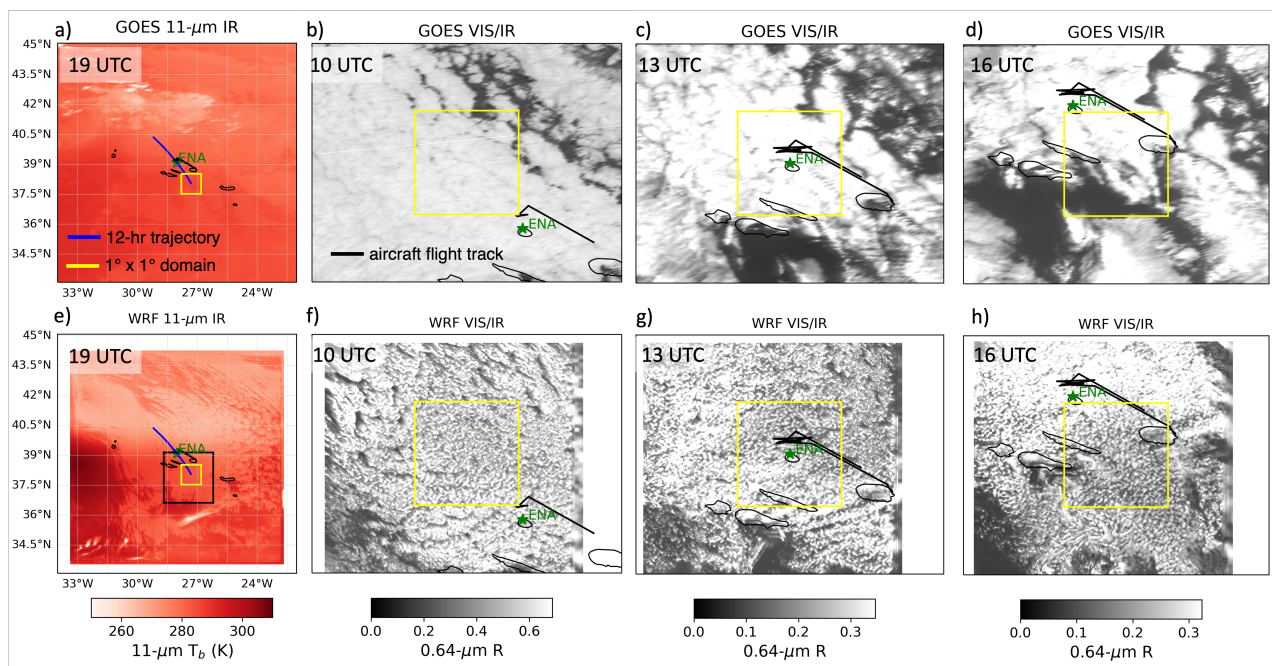
Figure 3. GOES 11-μm thermal infrared image at 07/18/2017 at 19:00 UTC centered over the Graciosa island with the positions of along the HYSPLIT trajectory computed using ERA5 reanalysis is plotted in blue a). The yellow box denotes a $1 \times 1°$ region that moves along the center of the trajectory. Visible imagery at 0.64-μm reflectance over a larger $2 \times 2°$ region is shown at discrete times (10, 13, and 16 UTC; b, c, d respectively). Similarly, the WRF brightness temperature at 11 μm and normalized shortwave albedo is displayed at the same times (e, f, g, and h). The black line denotes aircraft observations from the ACE-ENA campaign.
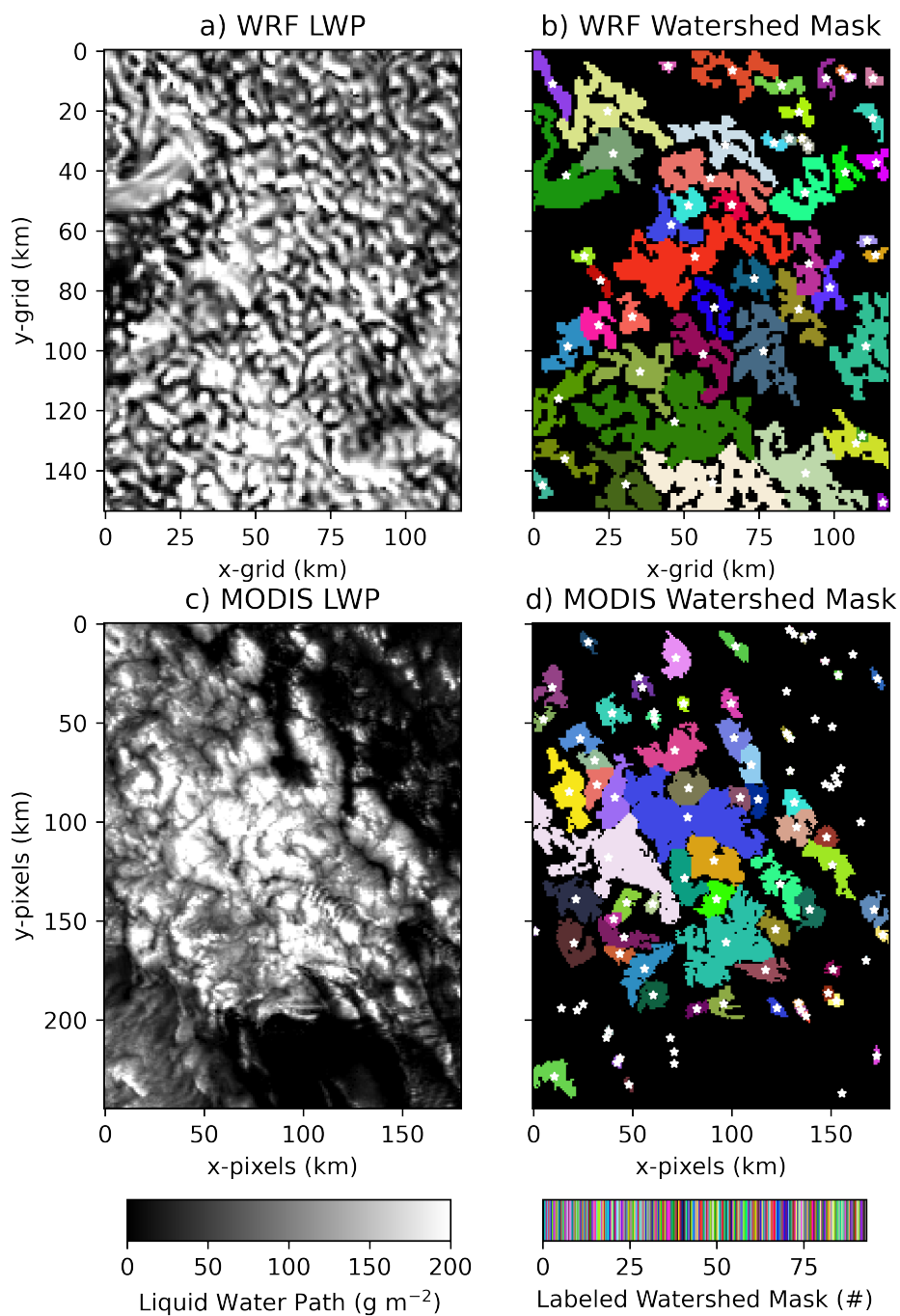
Figure 4. Liquid water path and watershed regions for WRF (a and b) and MODIS (c and d) in the case study occurring on 07/18/2017 at 13 UTC.
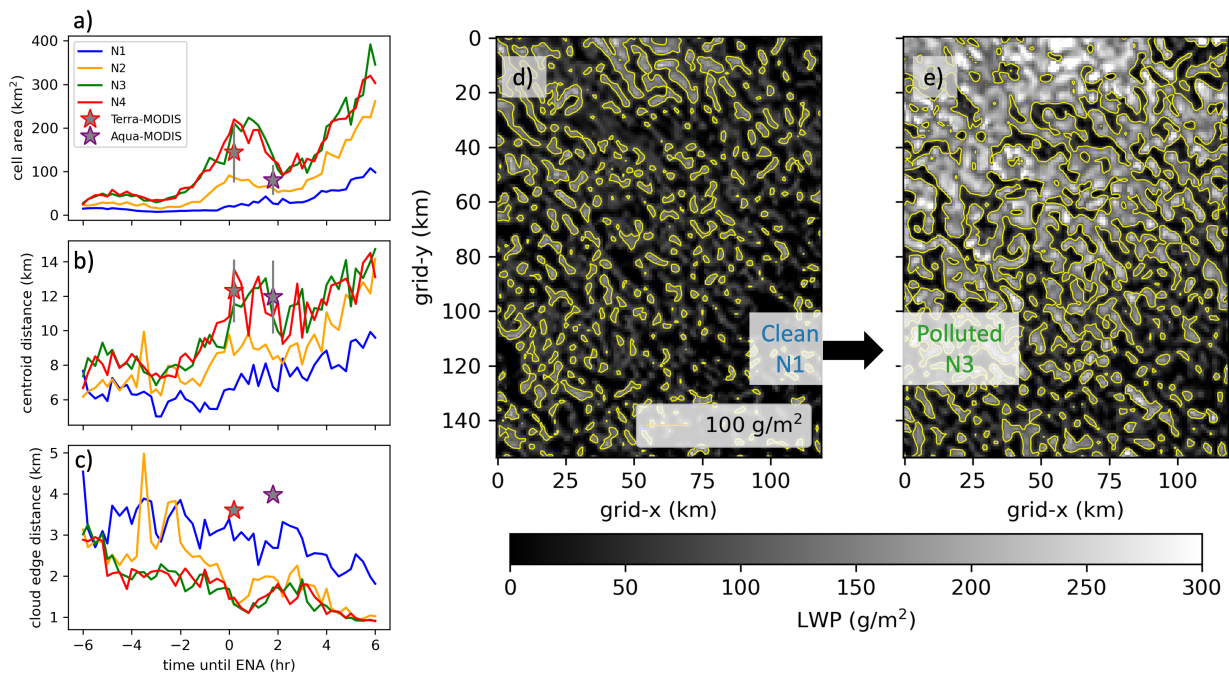
Figure 5. Time-series of the average (a) cloud object area, (b) minimum distance between cloud centroids, (c) minimum distance between cloud edges over each 15-minute time-interval detected for ultra clean (blue), clean (orange), control (green), and polluted (red) experiments in the case study occurring on 07/18/2017. MODIS averages (star) and standard deviations (vertical lines) are displayed on the image. LWP at 13 UTC is displayed for the clean (d) and polluted experiments (e).
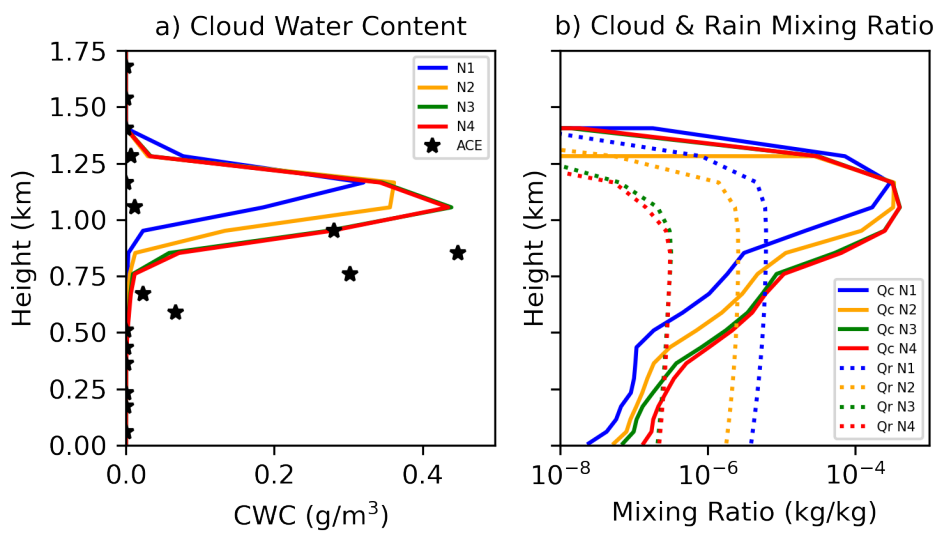
Figure 6. a) Vertical profile of the cloud water content measured during the ACE-ENA flight (stars) on 07/18/2017 averaged over an hour across the domain from 13-14 UTC (path of the flight is shown in Figure 3 and simulated for pristine (N1; blue), clean (N2; orange), control (N3; green), and polluted (N4; red) experiments. b) Vertical profile of cloud (solid) and rain (dotted) water mixing ratios averaged over the domain for each aerosol experiment.
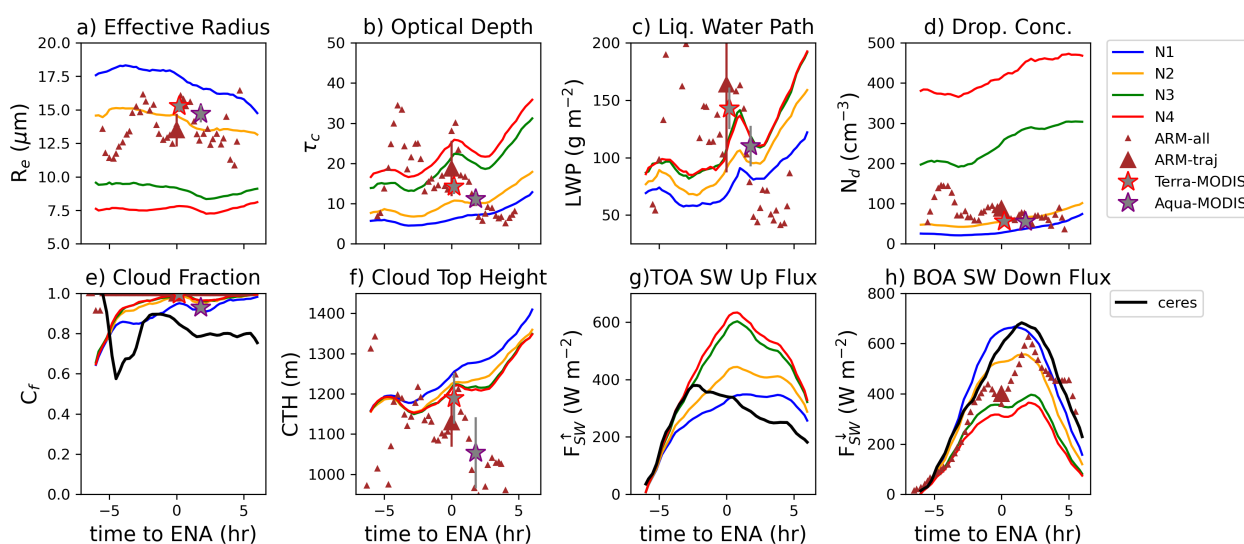
Figure 7. a) Droplet effective radius, b) cloud optical thickness, c) liquid water path, d) droplet concentration, e) liquid cloud fraction, f) cloud top height (CTH), g) top of atmosphere outgoing shortwave radiative flux ($F_{SW}^{\uparrow}$, and h) bottom of atmosphere incoming shortwave flux ($F_{SW}^{\downarrow}$ for pristine (blue), clean (orange), control (green), and polluted (red) WRF simulations. WRF-Solar was used for comparison with the satellite retrievals. ARM (brown diamond) retrievals are provided at all time steps and at the time when the trajectory passes over the ARM site (larger brown diamond) and MODIS retrievals from satellites Terra (red star) and Aqua (blue star) are provided when available along the trajectory on 07/18/2017. Note, aside from time to ENA equals 0, the ARM measurements do not coincide with the trajectory location and are merely used to show Eulerian variability.
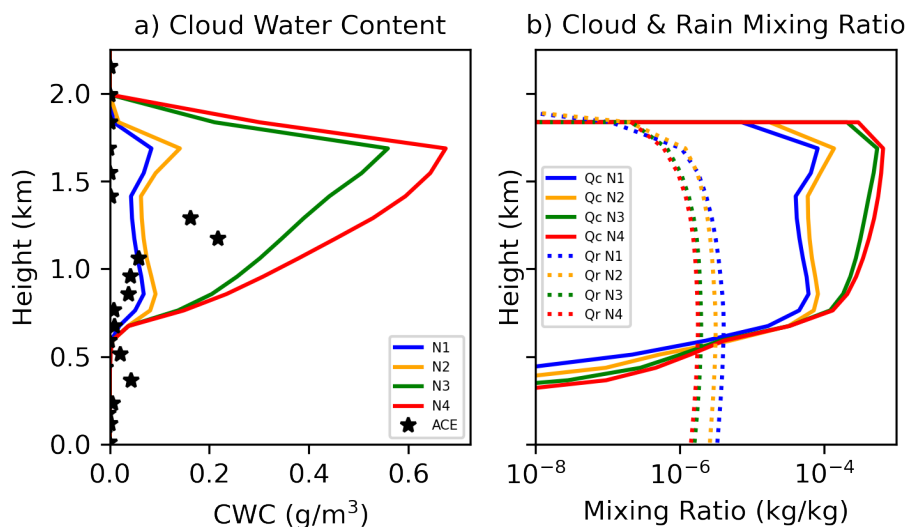
Figure 8. a) Vertical profile of the cloud water content measured during the ACE-ENA flight (stars) on 07/15/2017 averaged over an hour across the domain from 13-14 UTC (path of the flight is shown in Figure 3 and simulated for pristine (N1; blue), clean (N2; orange), control (N3; green), and polluted (N4; red) experiments. b) Vertical profile of cloud (solid) and rain (dotted) water mixing ratios averaged over the domain for each aerosol experiment.
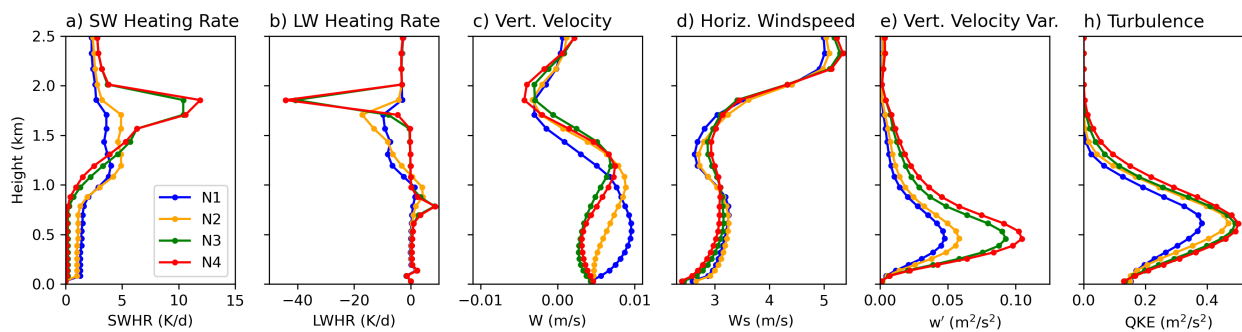
Figure 9. Vertical profile of the a) mean shortwave and b) longwave radiative heating rate, c) mean vertical velocity, d) mean horizontal wind speed, e) vertical velocity variance, and h) 2-times the turbulent kinetic energy (TKE; QKE is twice the TKE) for pristine (blue), unpolluted (orange), control (green), and polluted (red) WRF simulations on 07/15/2017 at 13:00 UTC.
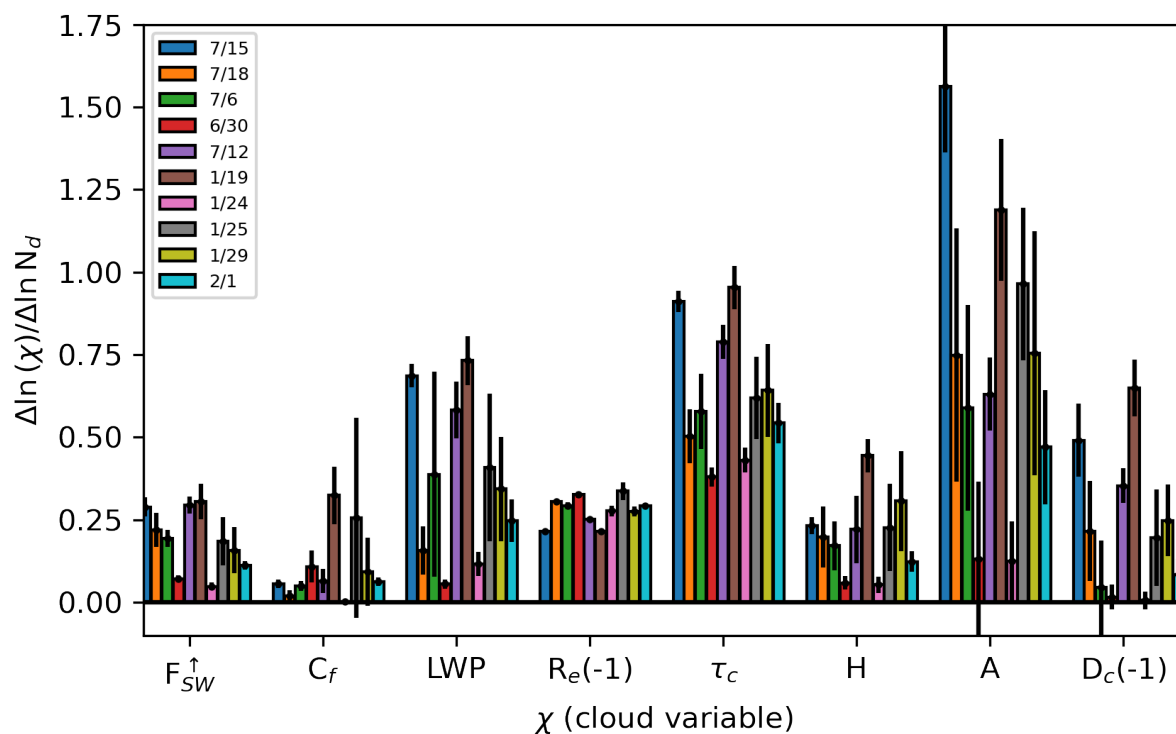
Figure 10. Value of the slope in the natural log change of a given variable (χ) with to the natural log change in cloud droplet number concentration (N_d) computed from 4 aerosol WRF experiments simulations in 10 different case studies (7/15, 7/18, 7/6, 6/30, 7/12, 1/19, 1/24, 1/25) represented at 13:00 UTC. χ variables shown are the top of atmosphere outgoing shortwave flux ($F_{SW}^{\uparrow}$), liquid cloud fraction (C_f), liquid water path (LWP), effective droplet radius (R_e), cloud optical thickness (τ_c), cloud geometrical thickness (H), cloud object area extent (A), and distance between cloud object centroids (D_c). Multiplication of -1 on R_e and D was carried out to make all quantities positive across the bar chart. Uncertainties are represented by the 1-sigma error of the regression fit between quantities.
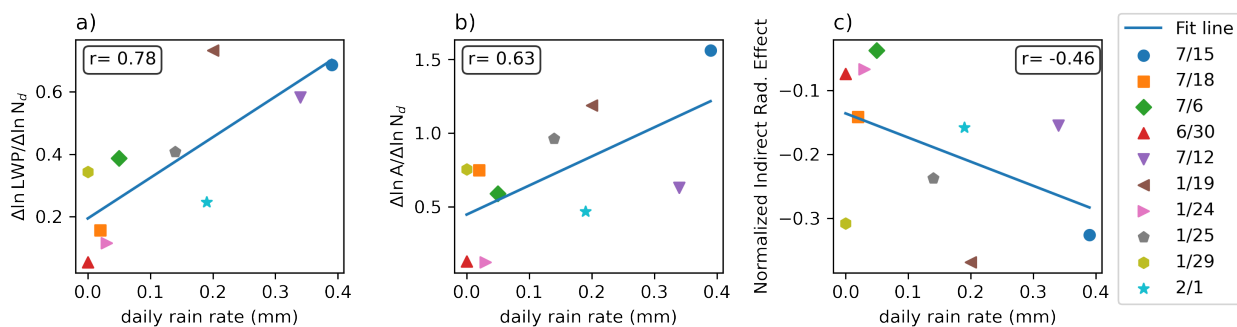
Figure 11. Scatter plot of the a) change in liquid water path ($\frac{\Delta \ln L}{\Delta \ln N_d}$), b) change in cellular cloud area as a function of N_d and c) normalized indirect radiative effect which constitutes the Twomey + $\mathrm{LWP}_{adj.}$ + $\mathrm{CF}_{adj.}$ as a function of daily accumulated rain rate from ARM for simulations $\pm$ 3 hours from the time the trajectory intersects Graciosa Island for each case study day, designated by a different symbol as shown in the legend.
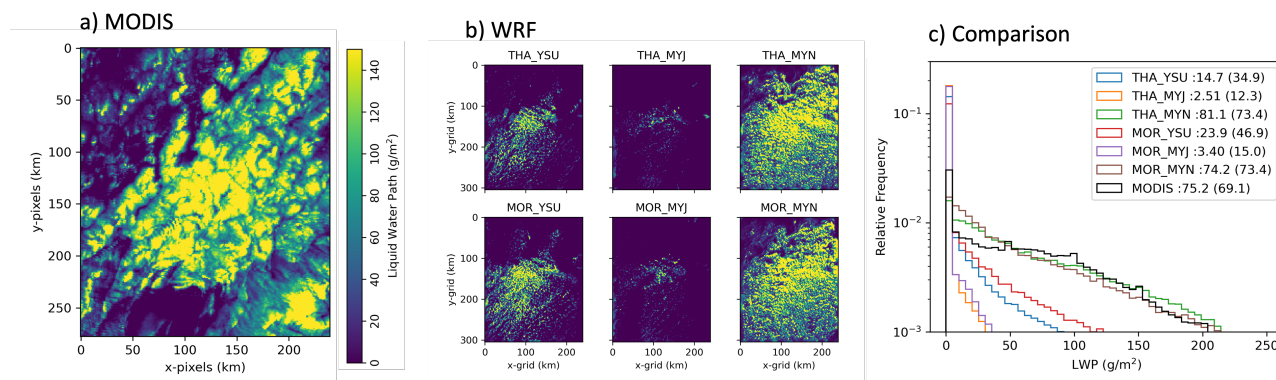
Figure 12. WRF control experiments using combinations of the Thompson (THA), Morrison (MOR), Yonsei University (YSU), Mellor–Yamada–Janjic (MYJ), and Mellor-Yamada-Nakanishi-Niino (MYN) boundary layer schemes. Spatial distributions of the liquid water path is shown over the (a) MODIS retrieval of liquid water path at 3.7-μm at 14:40 UTC, (b) WRF inner domain at 13:00 UTC, and (c) a histogram of the LWP for each experiment and MODIS data. Values in the legend of (c) represent means and standard deviations for each experiment combination.

Table 1. WRF model schemes used to study aerosol-cloud interactions. Values for the coinciding names denote the option number used in WRF.

WRF scheme	Value	Name
microphysics	28	Thompson (aerosol-aware)
radiation	4	RRTGM
cumulus	6	Tiedtke
pbl	6	MYNN
sfclay_physics	2	eta similarity
surface physics	2	Noah Land

Table 2. Case studies from ACE-ENA IOP periods used to simulate stratocumulus clouds in WRF. Surface temperature (T_s), lower troposphere static stability (LTS), free troposphere entraining relative humidity at 850hPa (FTH), PBL height (determined from the temperature and humidity sounding), cloud base height (determined from the ceilometer), and daily integrated rainfall determined from ARM distrometer observations. Dominant cloud type following Wood and Hartmann (2006) classification based on satellite imagery inspection are listed.

	T_s [°C]	LTS [K]	FTH	PBL height [m]	Cloud base height [m]	Rainfall [mm]	Cloud type	Precipitation
IOP 1								
6/30/17	20.0	20.0	36	890	950	0	disorganized	non-raining
7/06/17	21.5	20.2	26	1410	1107	0.05	homogeneous	light-rain
7/12/17	22.0	17.2	72	1130	325	0.34	homogeneous	moderate rain
7/15/17	16.0	22.0	60	1530	850	3.9	homogeneous	heavy-rain
7/18/17	22.0	18.2	63	950	682	0.02	closed-cells	non-raining with overlying cloud layers
IOP 2								
1/19/18	16.5	16.0	52	950	816	0.2	open-cells	rain
1/24/18	14.0	18.0	32	1710	1411	0.03	open-cells	light-raining with ice
1/25/18	13.0	19.7	21	1510	1302	0.14	closed-cells	drizzle with ice
1/29/18	15.0	18.1	50	1200	1062	0	disorganized	non-raining
2/01/18	15.0	17.8	41	600	565	0.19	disorganized	drizzle

Table 3. Twomey radiative effect and ratio of the liquid water path adjustment and cloud fraction adjustment to the Twomey effect computed using equation 1 for each case study. Mean values across all case studies and all case studies excluding 1/25 due to excessive cloud growth by aerosol are included in the last two rows.

Case	Twomey (W m^{-2})	$\frac{LWP_{adj}}{Twomey}$	$\frac{C_{fadj}}{Twomey}$
7/15/17	-107.5	1.47	0.55
7/18/17	-98.3	0.38	0.05
7/6/17	-20.7	0.13	0.69
6/30/17	-54.2	0.14	0.24
7/12/17	-92.0	0.48	0.21
1/19/18	-49.5	1.61	0.61
1/24/18	-23.0	0.31	0.015
1/25/18	-17.6	0.74	4.85
1/29/18	-37.0	1.59	1.65
2/1/18	-39.4	0.57	0.55
Mean (all)	-53.9 ± 10.6	0.74 ± 0.55	0.94 ± 1.37
Mean (excluding 1/25)	-57.9 ± 11.0	0.74 ± 0.6	0.51 ± 0.47

Table 4. WRF model setup for control and sensitivity experiments. Values in parenthesis denote the option number used in WRF. Experimental setup primarily used for analysis of detailed aerosol-cloud interaction experiments is listed in bold.

Experiment name	Microphysics	PBL
THA_YSU	Thompson (28)	YSU (1)
THA_MYJ	Thompson (28)	MYJ (2)
THA_MYN	Thompson (28)	MYNN3 (6)
MOR_YSU	Morrison (10)	YSU (1)
MOR_MYJ	Morrison (10)	MYJ (2)
MOR_MYN	Morrison (10)	MYNN3 (6)